nature communications

Article

https://doi.org/10.1038/s41467-025-59590-9

Reactive oxygen species responsive nanomotors for gene edited metabolic disruption and immunotherapy

Received: 8 July 2024

Accepted: 29 April 2025

Published online: 21 May 2025

Check for updates

Zhiyong Liu[1,3], Xiaowei Luan[1,3], Qianglan Lu[1], Shurong Qin[1], Fei Zeng[1], Zhi Li[1], Bangshun He[2] & Yujun Song[1]

While gene-editing-based tumor therapy holds promise, conventional passive-diffusion vectors face limited penetration in dense solid tumors. Here, we developed a ROS-driven gene editing nanomotor (RDN@PL), which takes hemin as the core and encapsulates CRISPR/Cas9 plasmids targeting LDHA (A glycolysis key enzyme). In tumor microenvironments, RDN@PL consumes extracellular ROS to fuel self-diffusiophoresis, achieving higher intratumoral accumulation than passive particles. Upon internalization, heme oxygenase-1 (HO-1) degrades RDN@PL, releasing CO and plasmids. LDHA knockout suppresses glycolysis while CO elevates mitochondrial ROS, which triggers apoptosis by disrupting metabolism and enhancing immunity. Simultaneously, extracellular ROS depletion by non-internalized nanomotors reverses immunogenic cell death (ICD) inhibition, enhancing CD8+ T cell infiltration in tumor. The Janus nanomotor enables extracellular ROS scavenging and intracellular ROS increment via HO-1-responsive cargo release and gene editing. This multi-level intervention strategy demonstrates 93.9 % tumor growth suppression in solid tumor models, providing a blueprint for engineering intelligent nanovesicles in precision oncology.

As an efficient and precise gene editing tool, clustered regularly interspaced short palindromic repeats (CRISPR)-associated protein 9 (Cas9) has become a common strategy for the treatment of major diseases, such as tumors and neovascular diseases, guided by single guided RNA (sgRNA), Cas9 proteins can knock out target sequences within hours[1–3]. Numerous studies have been conducted to deliver RNP or plasmid encoding the Cas9 system via cationic polymers, such as PEI[4], chitosan[5], liposome[6] etc., to complete the gene editing process after endocytosis by the cells. However, the low delivery efficiency has been a barrier to its clinical application. Overcoming complex physiological barriers to enter target cells is the first step for gene editing. In recent years, as researchers perceive the potential of bio-nanomaterials in the field of oncology therapy, various nanomaterial-based CRISPR/Cas9 editing systems, such as antibody protein modification[7], external stimulation[8,9], and tumor microenvironmental response[10], have been proposed, with the expectation of enhancing the uptake of the Cas9 system by tumor cells and completing the editing process of target genes in a precise and controllable manner. Despite the promising prospects, most of the strategies still follow the traditional delivery strategy based on nanoparticle's passive diffusion, which usually faces challenges due to the dense and complex micro-environment of solid tumors. Therefore, innovative delivery strategies are urgently needed to enhance the delivery and editing efficiency of CRISPR/ Cas9 to target cells.

Micro/nano motors are micro/nano-sized particles that can convert chemical or external field energy into mechanical energy[11–13]. Typically, the asymmetric Janus morphology endows the micro/nano motors with stronger directional motility versus passively diffusing

[1]Department of Gastric and Hernia Surgery, Nanjing Drum Tower Hospital, College of Engineering and Applied Sciences, State Key Laboratory of Analytical Chemistry for Life Science, Nanjing University, 210023 Nanjing, China. [2]Department of Laboratory Medicine, Nanjing First Hospital, Nanjing Medical University, 210006 Nanjing, China. [3]These authors contributed equally: Zhiyong Liu, Xiaowei Luan. e-mail: ysong@nju.edu.cn

particles. Benefiting from their ability of autonomous locomotion, micro/nano motors have been utilized to implement interesting intelligent operations such as cargo delivery[14,15], non-invasive surgery[16,17], target molecule capture[18], physiological barrier crossing[19], etc., and have been highly acclaimed in the fields of signal detection[20,21], disease treatment[22,23]. Due to the microscopic controllability, the nanoscale devices can be carefully designed to produce surprising effects, such as efficient crossing of the blood-brain barrier and strong penetration into dense tissues[24,25], etc. Recently, some studies have verified that nanomotors have catalytic reaction-dependent high concentration substrate tropism, named chemotaxis, which suggested new ideas for intelligent targeted delivery of nanomotor[26–28]. Furthermore, the autonomous motility of the nanomotors allows for better cellular uptake and lysosomal escape, which is critical for the CRISPR/Cas9 system delivery. Therefore, such autonomous moving vectors are expected to endow CRISPR/Cas9 gene editing systems with interesting applications and provide better candidates for tumor nanotherapeutic platforms.

Distinct from the metabolic processes of normal cells, tumor cells reprogram their metabolic processes because of the Warburg effect to adapt to the energy and material consumption during rapid proliferation, including lactic acid metabolism and reactive oxygen species (ROS) production[29–31]. Lactate, an important product of the Warburg effect in tumor cells, has been demonstrated to promote tumor glycolysis and immunosuppression. It is converted to pyruvate and participates in the metabolic cycle under the action of lactate dehydrogenase A (LDHA)[32,33]. Inhibition of lactate level has become an effective pathway for tumor metabolism and immunotherapy[34–37]. Additionally, as a product of mitochondrial respiration, ROS plays a crucial role in the life activities of tumor cells and is involved in the regulation of cell proliferation[38–40]. Recent studies have shown that one of the gas signaling molecules, carbon monoxide (CO), significantly upregulates ROS lethality in tumor cells[41–43]. The therapeutic strategy of using exogenous CO donors, such as Mn_2CO_{10}[44], $Fe(CO)_5$[45], to induce explosive release of ROS from tumor cell mitochondria to destroy tumor cells has been widely accepted, although their biotoxicity is a concern.

Furthermore, as an important immune regulatory mechanism, immunogenic cell death (ICD) of tumors can induce anti-tumor effects through the release of various immunogenic factors (HMGB1, CRT, etc.)[46]. However, as the product of the unique metabolism of tumor cells and some anti-tumor treatment processes, the ROS overexpressing in the tumor microenvironment rapidly oxidizes HMGB1 secreted into the extracellular matrix, and destroys the immunogenicity of that, leading to the blockage of the chemotaxis and maturation of immune cells such as dendritic cells (DCs)[47,48] and weakening the effectiveness of immunotherapy ultimately. Therefore, inhibiting the level of ROS outside the tumor cells seems to be a key approach to enhance both oxidative damage death and immunotherapy of tumor cells.

In this work, we developed a nanomotor that utilizes ROS in the tumor microenvironment as fuel for targeted gene editing with CRISPR plasmids (Fig. 1). Formed by self-assembly of amphiphilic oligomers of chitosan-hemin (Cs-He) and chitosan-palmitic acid (Cs-Pa), the nanomotor was designed to actively target tumor cells induced by the ROS gradient, enabling efficient cargo delivery, cellular uptake, and lysosomal escape. Externally, the core component, hemin, can rapidly degrade extracellular ROS, alleviating ICD inhibition due to extracellular ROS accumulation. Upon cellular uptake, hemin is catabolized by tumor cell overexpression of heme oxygenase-1 (HO-1)[49,50], releasing CO and converting to water-soluble bilirubin (Bi)[51,52], which can result in the tumor-responsive release of the plasmid. When the released plasmids are expressed, the CRISPR/Cas9 protein can knock out LDHA locus, inhibit tumor cell glycolysis, enhance mitochondrial activity, and generate the intracellular ROS storm. The low LDHA expression will reduce lactate in tumor cells, thereby alleviating immune microenvironmental suppression. Additionally, endogenous CO can effectively promote endothelial cell growth, facilitating normalization of the tumor vasculature and optimizing the immune microenvironment. The Janus nanomotor in this study achieved the opposite regulation of intra/extracellular ROS, which have a form-effect integrated dual Janus property, and realized tumor metabolic interference and enhanced immunotherapy. This strategy provided a new option for CRISPR/Cas9 targeting delivery and tumor treatment.

Result

Preparation and characterization of RDN@PL

Two amphiphilic oligomer molecules, chitosan-hemin (Cs-He) and chitosan-palmitic acid (Cs-Pa), were synthesized by a simple EDC/NHS reaction (Supplementary Fig. 1), and the successful preparation of Cs-He and Cs-Pa was characterized by FT-IR (Supplementary Fig. 2) and H-NMR spectra (Supplementary Figs. 3, 4). The telescopic vibrational peaks of the carboxyl groups in the hemin and palmitic acid molecules at 1700 cm^{-1} wave number were red-shifted towards 1660 cm^{-1} after the reaction, indicating the successful formation of amide bonds. In addition, high-resolution mass spectrometry (HRMS) revealed a proportional coupling of the two components in the Cs-He and Cs-Pa molecules (Supplementary Figs. 5, 6). The hybrid vehicles were prepared by hydrosonic ultrasonication after mixing Cs-He and Cs-Pa, as shown in the transmission electron microscopy (TEM) images of Fig. 2a and Supplementary Fig. 7. At the initial stage of vesicle formation, the different components were mixed homogeneously, constituting nanovesicles with symmetric morphology. However, the hemin molecules in the vesicles aggregated by π-π stacking, and this stronger interaction excluded the other hydrophobic fragment Pa and produced phase separation, which could be clearly observed under TEM after about 6 h. This unstable structure gradually developed with the extension of time and eventually became stable Janus particles with outgrowth structure. Because the gradual development of the self-assembly process of the vesicle structure leads to changes in surface components and particle morphology, the whole process was accompanied by changes in zeta potential of the particle and was completed in about 72 h (Fig. 2a and Supplementary Fig. 8). UV–Vis absorption spectrum showed that ROS-driven nanomotor (RDN) has a characteristic absorption peak at 400 nm, identifying the presence of hemin (Fig. 2b). The concentration of Fe element was determined by inductively coupled plasma (ICP) to measure the content of hemin in each component, which accounts for 49.7 % and 41.2 % in Cs-He and RDN, respectively (Supplementary Fig. 9). Furthermore, we loaded the plasmid encoding the CRISPR-Cas9 system by electroporation (Plasmid information is shown in Supplementary Fig. 10), the results of DNA gel electrophoresis were shown in Fig. 2c, and RDN was very effective in loading plasmid, and the plasmids were encapsulated by the RDN completely at the N/P ratio of 3. The changes in loading rate and encapsulation rate with mass ratio were shown in Fig. 2d. In addition, simple co-mixing of RDN with the plasmid had a lower loading efficiency, although the product had a similar surface potential, which ruled out the possibility that the plasmid was adsorbed on the surface of the hybrid vesicle without being encapsulated internally (Supplementary Fig. 11). We chose the condition of mass ratio at 1 to synthesize the subsequent RDN@PL, with the loading rate and encapsulation efficiency of 51.2 % and 52.3 % respectively, and the stable nanostructures could be observed by TEM (Fig. 2e). Element mapping results showed the regular vesicle structure of RDN@PL as well as the unilateral distribution of Fe elements, while the P element representing the plasmid showed a clear internal encapsulation (Supplementary Fig. 12). Dynamic light scattering results showed that RDN had a significant size change (from 216.7 nm to 249.8 nm) after loading the plasmids (Fig. 2f), in addition, the zeta potential shifted from 25 mV to

https://doi.org/10.1038/s41467-025-59590-9

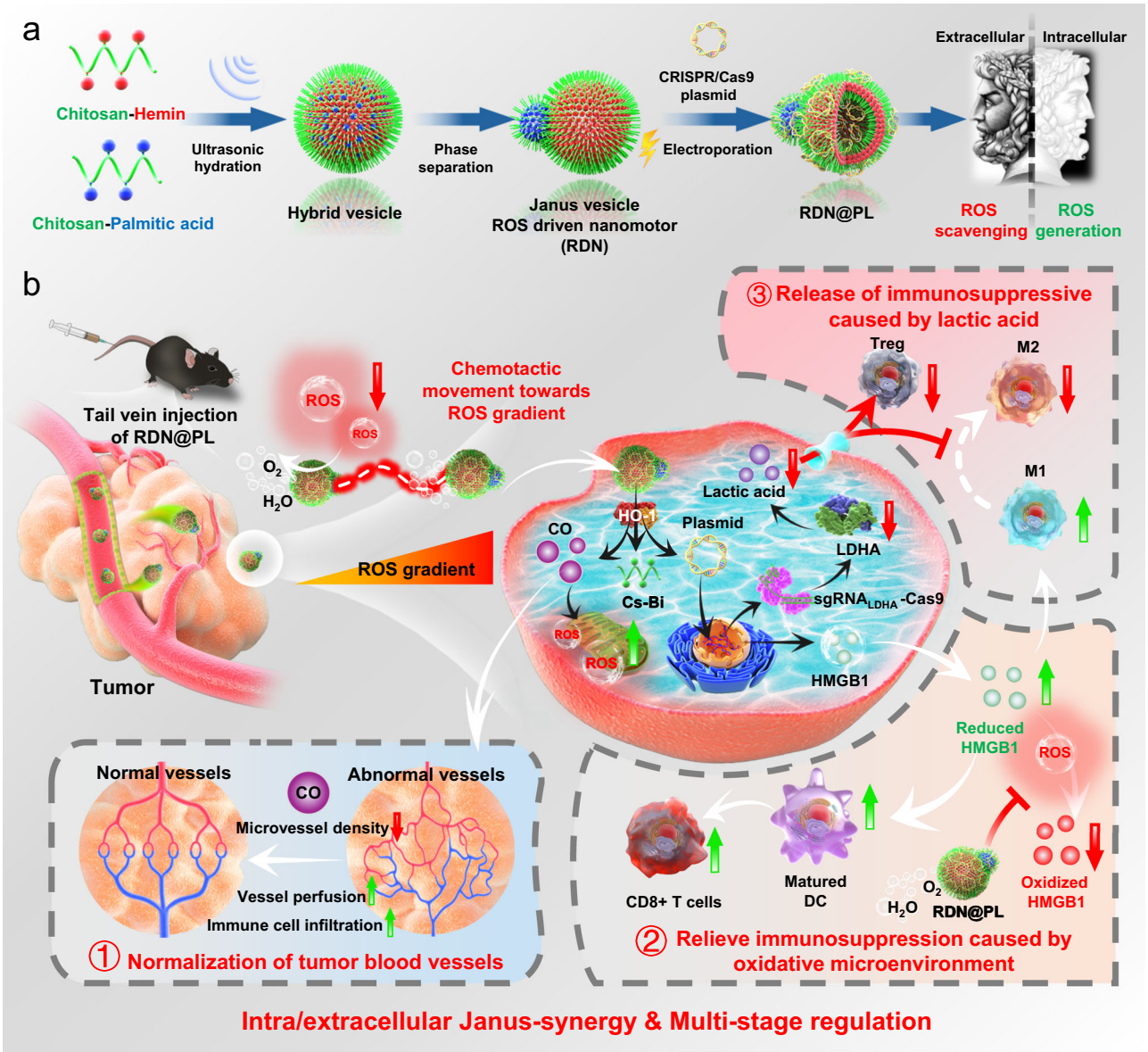

Fig. 1 | Schematic illustration for the preparation of ROS-driven nanomotors (RDN@PL) and the intra/extra-cellular Janus regulation for tumor metabolism intervention and immunotherapy strategies. a Schematic illustration of the synthesis of RDN@PL. The RDN was prepared by self-assembly of amphiphilic molecules. Hybridized vesicles undergo phase separation and generate Janus structures due to π-π stacking of hemin after a period of resting. The CRISPR/Cas9 plasmid targeting LDHA was subsequently loaded in RDN by electroporation to obtain RDN@PL. **b** Schematic illustration of the synergistic solid tumor therapy that extracellular regulation and intracellular metabolic disruption by RDN@PL. Relying on ROS-chemotaxis to be internalized, RDN@PL responsively generate CO in tumor cells and release CRISPR/Cas9 plasmids to promote mitochondrial ROS storms synergistically. Extracellularly, RDN@PL depleted ROS sustainedly to mitigate the oxidative microenvironment, synergizing with LDHA knockout-induced lactate downregulation and CO-induced vascular normalization for enhanced antitumor immunity.

−8 mV (Fig. 2g). The significant change in size and potential may be a joint result of the static point adsorption of the plasmid by the abundant amino groups on the surface of Cs and the encapsulation of the vesicle cavity.

Subsequently, the H_2O_2-catalyzed kinetics of RDN@PL were examined, as shown in Fig. 2h and Supplementary Fig. 13. Due to the strong hydrophobicity of hemin, which agglomerates in aqueous solution, it is difficult for H_2O_2 to enter into the interior of its active site to react, resulting in a low catalytic reaction rate. However, after chemical modification by Cs, RDN was uniformly dispersed in an aqueous solution, leading to a significant enhancement in catalytic efficiency. The V_{max} and K_M reached 2.10×10^{-7} M s^{-1} and 6.37 mM, respectively. Furthermore, RDN@PL retained most of its catalytic activity after plasmid loading (V_{max} = 2.42×10^{-7} M s^{-1}, K_M = 6.59 mM), and which strongly supports the self-diffusiophoresis of nanomotors. The reproducibility and dimensional stability of the RDN@PL were further determined. The universal cationic transfection reagent Lipo-some2000 was used to load the plasmid and constitute Liposome@PL as the control. Different batches of RDN@PL were synthesized with similar hydration sizes, which validates the high reproducibility of the synthesis strategy (Supplementary Fig. 14a). Furthermore, RDN@PL shows the surprising long-term stability, which has a clear advantage over liposome due to its strong self-assembly based on π-π conjugation and its ability to be preserved in PBS and 10% FBS for more than 1000 h at 37 °C without noticeable dimensional and potentiometric changes (Supplementary Fig. 14b–e). The janus morphology of RDN@PL dispersed in FBS remains remarkably intact after 1500 h (Supplementary Fig. 14f).

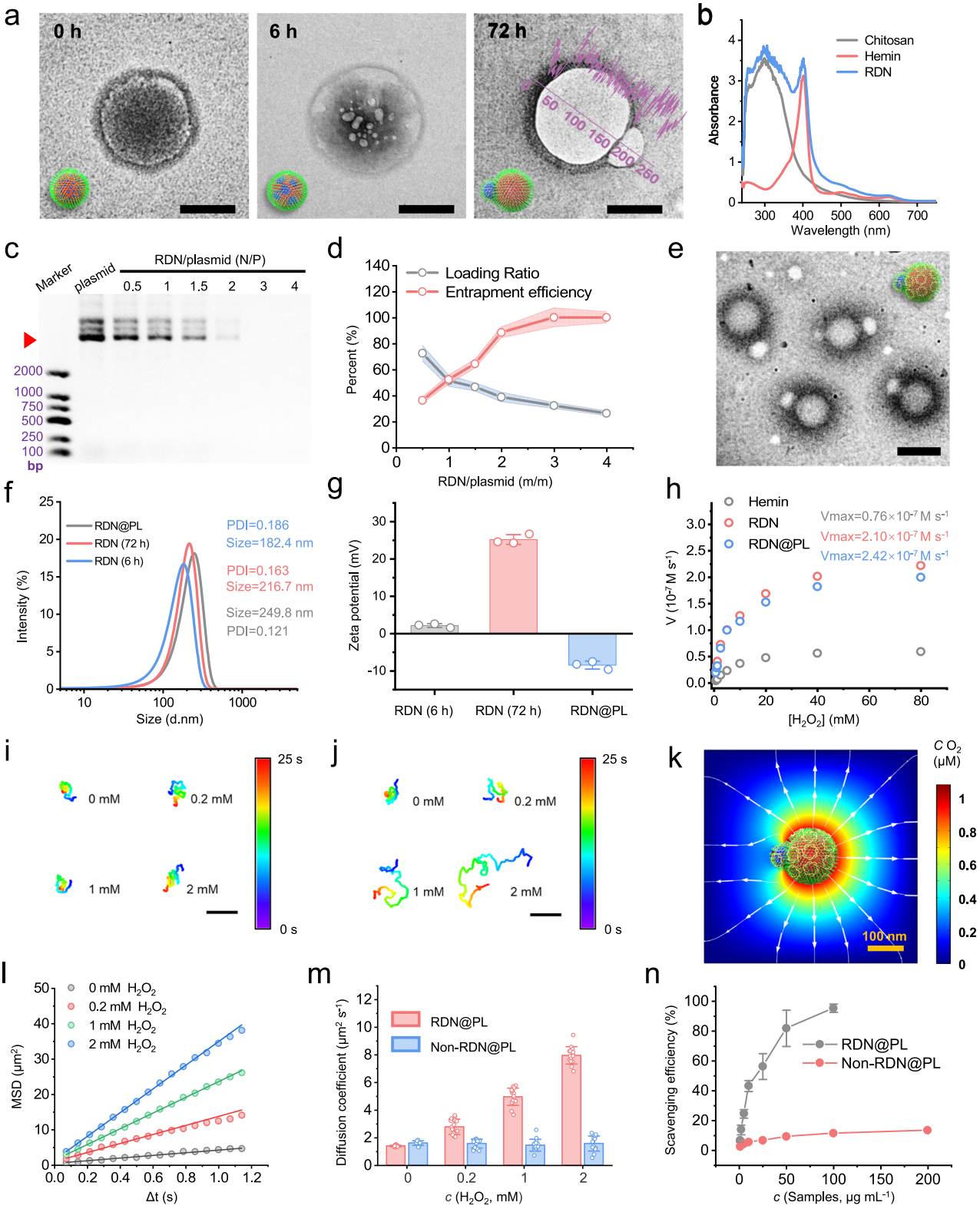

Protoporphyrin (Pp), without ROS catalytic activity, served as a control for hemin in the synthesis of Non-RDN@PL (Supplementary Fig. 15). The successful synthesis of the different components was confirmed through the similar characterizations (Supplementary Fig. 16a, b), while the TEM images demonstrated a Janus structure similar to that of RDN@PL (Supplementary Fig. 16c). However, Non-RDN@PL lacks the catalytic properties as RDN@PL obviously (Supplementary Fig. 17a, b). Bright-field microscopy recordings and analyses of Non-RDN@PL and RDN@PL's motion in H_2O_2 solution (Supplementary Movies 1 and 2). Non-RDN@PL remained in Brownian motion, driven by molecular thermal force, even in 2 mM H_2O_2 solution, due to the absence of catalytic drive, while the motion trajectory of RDN@PL exhibited significant self-driving behavior with changes in H_2O_2 concentrations, as depicted in Fig. 2i, j. The finite element simulations were implemented to gain a deeper understanding of RDN@PL's motion mechanism, exemplified in Fig. 2l and

Fig. 2 | Preparation, catalysis and motion properties characterization of RDN@PL. a TEM images of morphological changes over time after the formation of RDN vesicles (Scale bar: 100 nm). The experiment was repeated independently three times with similar results, and a representative result is shown. **b** UV–Vis absorption spectra of different samples. **c** The DNA gel electrophoresis image of the free plasmids after electroporation, the concentration ratio is RDN to plasmid (N/P), and (**d**) The encapsulation efficiency and loading ratio of plasmids in RDN@PL (n = 3 independent experiments). **e** The TEM image of RDN@PL (Scale bar: 200 nm). The experiment was repeated independently three times with similar results, and a representative result is shown. **f** The hydration diameter and (**g**) zeta potential of different particles (n = 3 independent experiments). **h** Steady-state kinetic assay of different particles for the catalyzation of H_2O_2. The motion trajectories of (**i**) Non-RDN@PL and (**j**) RDN@PL recorded by bright field microscope (Scale bar: 10 μm). **k** Finite element simulation for the catalytic reaction of RDN@PL, which considers the release site, production rate, and diffusion rate of O_2. **l** The Mean square displacement (MSD) of Non-RDN@PL and RDN@PL versus time interval (Δt) in H_2O_2 solution with different concentrations. **m** The diffusion coefficients statistical analysis of particles in H_2O_2 solution (n = 15 independent experiments). **n** The clearance efficiency of Non-RDN@PL and RDN@PL for ·OH within 30 min (n = 3 independent experiments). Data are presented in the form of mean values ± standard deviation (SD). Source data are provided as a Source Data file.

Supplementary Fig. 18. When RDN@PL catalyzes the decomposition of H_2O_2, the production of O_2 molecules increases the overall quantity of matter present in the reaction system. The distribution of hemin in Janus morphology of RDN@PL is geometrically asymmetrical. Once the catalytic reaction reaches a steady state, the O_2 concentrations become asymmetrical around the RDN@PL particles, causing the particles to display self-diffusiophoresis motion. Figure 2l and Supplementary Fig. 19 display the mean square displacements (MSD) of RDN@PL and Non-RDN@PL over time intervals (Δt) in H_2O_2 solution, which depicts that RDN@PL exhibited a significant self-diffusiophoresis motion. Because of the lack of catalytic activity towards H_2O_2, Non-RDN@PL did not show significant motility phenomena, implying that it is a suitable control group for the following validation of motility effect. Additionally, the equivalent diffusion coefficients (D_{eff}) were determined via the MSD. RDN@PL displayed robust movements in the presence of substrate H_2O_2, with its D_{eff} reaching approximately 5-folds that of Brownian motion particles at a H_2O_2 concentration of 2 mM (Fig. 2m). It is worth mentioning that H_2O_2 was used as the substrate for the reaction to elucidate the motility mechanism of RDN@PL. However, as the catalytic component of RDN, hemin can react with a range of reactive oxygen species, including H_2O_2, ·OH, and $\cdot O_2^-$, which play important roles in tumor progression. We examined the scavenging effect of RDN@PL on ·OH, the most oxidative ROS. As illustrated in Fig. 2n, 100 μg mL^{-1} of RDN@PL was able to scavenge 95.4% of ·OH within 30 min, highlighting its potential as an effective ROS scavenger.

Intra/extra-cellular activities characterization of nanomotors

Chemotaxis, i.e. active movement towards a gradient of chemicals, is an important function of RDN@PL as a smart gene editing platform[53,54]. To verify the presence of a cell-scale ROS gradient, the Y-shaped microfluidic channel model was created through PDMS casting (Supplementary Fig. 20). B16F10 cells were inoculated in chamber a, and H_2O_2 produced by them was measured in different chambers (Supplementary Fig. 21). The ROS gradient was amplified with increasing channel distance, which indicates the presence of that at the cellular scale. With the substrate gradient, catalytically active nanoparticles will exhibit chemotactic behavior due to the turnover of substrate molecules[55,56], which is expected to drive cell-targeting movements of RDN@PL. As shown in Supplementary Fig. 22 and Movies 3–5, when dispersed in the cellular environment, Non-RDN@PL mainly made Brownian motion, and as a contrast, RDN@PL moves quickly and rapidly when approaching the cell. The directionality of the movement disappeared when the ROS was eliminated by NAC (N-acetylcysteine), which demonstrated the ROS gradient-dependent chemotaxis of RDN@PL. Transwell co-culture plate was utilized to build an in vitro model to evaluate the Z-axis chemotactic effect of RDN@PL on tumor cells (Fig. 3a). Cy5.5-labeled particles were distributed uniformly in the upper and bottom chambers, followed by the cultivation of B16F10 cells in the upper chamber. The ROS gradient was subsequently formed in the perpendicular direction, causing the chemotactic movement of RDN@PL. As shown in Fig. 3b, the following 12 h of incubation induced by B16F10's metabolism to produce ROS, catalytically active RDN@PL was gradually transferred from the lower chamber to the upper chamber where B16F10 cells were located. The concentration increased to more than twice the initial concentration, indicating that RDN@PL could overcome gravitational force and complete the vertical chemotactic transfer of tumor cells. No similar result was observed in the Non-RDN@PL group.

Additionally, the 2D chemotaxis was evaluated in microfluidic channels. Various cargoes were then introduced into individual chambers to assess RDN@PL's ability to undergo planar chemotaxis and macrophage aggregation (Fig. 3c). The distribution of movement trajectories and steering angles observed at the Y-shaped bifurcation showed that RDN@PL was able to respond to the ROS gradient generated by B16F10 cells and swarm to chamber **b** (Fig. 3d and Supplementary Fig. 23). After introducing RDN@PL into **a** chamber for 12 h, the fluorescence intensity in **b'** was less than half of that in **b**, demonstrating the chemotactic aggregation ability of RDN@PL activated by B16F10 cells, rather than HUVECs (Fig. 3d), which was benefit for the remote active targeting and cargo delivery. Conversely, Non-RDN@PL exhibited homogeneous fluorescence intensity due to the passive diffusion effect spread equally across all chambers. As a crucial element of non-specific tumor immunity, macrophage activity holds great significance in tumor therapy. DiO-labeled macrophages were cultivated within the chambers **c** and **c'** to investigate the effects of RDN@PL on macrophage activity. Remarkably, after RDN@PL aggregation within the chambers containing tumor cells, macrophages situated in chamber **c** exhibited substantial directional migration ability towards the tumor cells. This effect was apparently attributed to the specific influence of RDN@PL prompting directional movement of macrophages. Further analysis of the detailed mechanism was explored subsequently.

Uptake efficiency has a great influence on the editing efficiency of the CRISPR/Cas9 system, and that of RDN@PL is expected to be further improved under self-diffusiophoresis and chemotaxis. As shown in Supplementary Fig. 24, the uptake efficiency of B16F10 cells and HUVECs on Non-RDN@PL and RDN@PL was quantitatively analyzed. RDN@PL rather than Non-RDN@PL was uptake by tumor cells for 12 h due to the ROS-mediated tumor cell chemotaxis, and the uptake efficiency was up to 22.1 %. The uptake of RDN@PL and Non-RDN@PL by HUVECs were both consistently low and without significantly difference. The uptake for Cy5.5-labeled different samples was observed by CLSM (Fig. 3e and Supplementary Fig. 25). The 3D view showed that RDN and RDN@PL (motion group) with self-diffusion ability were significantly internalized into the intracellular space by B16F10 cells, and their efficiency was higher than that of Non-RDN and Non-RDN@PL (Non-motion group), which indicated that the efficiency of the movement in the ROS environment of tumor cells gives it an excellent cell contact probability, thus contributing to its greater internalization by cells. In Supplementary Fig. 26, the cellular uptake pathway of RDN@PL was further validated. RDN@PL had a low cell uptake under 4 °C treatment, suggesting it was uptake by active transport of cells. The uptake efficiency was inhibited by about 40% when B16F10 cells were treated with the caveolin inhibitor (Genistein and methyl β-CD)[57,58], suggesting RDN@PL entered the cell by caveolin

https://doi.org/10.1038/s41467-025-59590-9

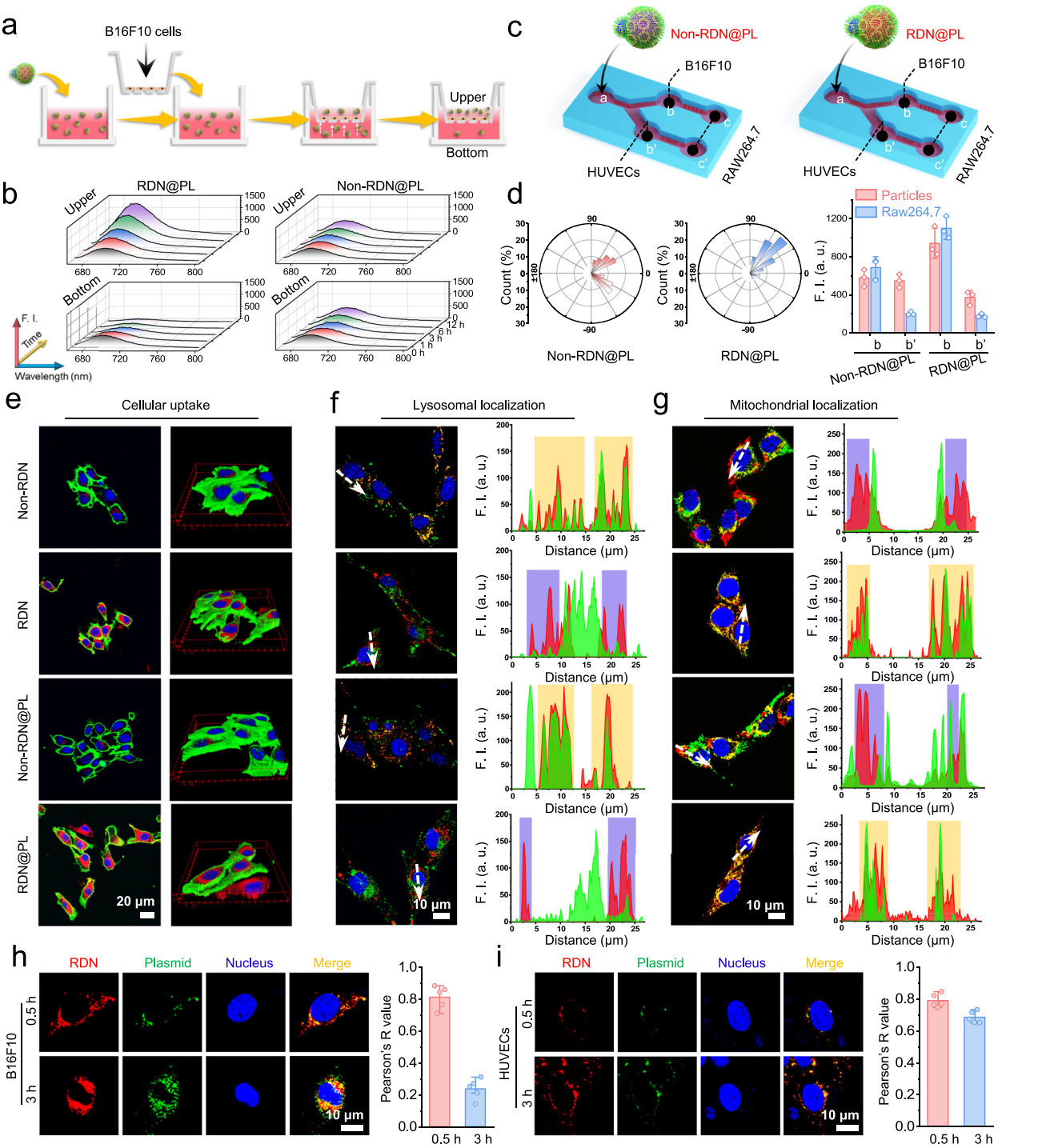

Fig. 3 | Chemotaxis and intracellular activity studies of RDN@PL on tumor cells. a Schematic illustration of the Transwell model to assess the *Z*-axis chemotaxis of RDN@PL towards B16F10 cells. **b** The fluorescence intensity representing particles content in the upper and lower chambers after treatment for different time ($t = 0, 1, 3, 6, 12$ h) in Transwell model. **c** Schematic illustration of the Y-shaped microchannel model to assess the *X*–*Y* axis chemotaxis of RDN@PL on B16F10 cells and chemotaxis induction on Raw264.7 cells. **d** The directional distribution of particles' movement trajectories at the channel bifurcation (Left, $n = 50$ independent samples) and the statistical analysis of fluorescence intensity in different chambers of Y-shaped microchannel (Right, $n = 3$ independent experiments). **e** The 2D (Left) and 3D (Right) CLSM imaging of different particles uptake by B16F10 cells after incubation for 6 h (Scale bar: 20 μm). CLSM images (Left, scale bar: 10 μm) and fluorescence co-localization analysis of (**f**) lysosomes and (**g**) mitochondria of B16F10 cells with Cy5.5-labeled particles after incubation for 3 h (Yellow rectangles in the histograms mark the fluorescence overlap areas, purple rectangles mark non-overlap areas). The CLSM images of RDN@PL in (**h**) B16F10 cells and (**i**) HUVECs (Scale bar: 10 μm), and the corresponding statistical analysis of Pearson's *R* value for co-localization ($n = 5$ independent experiments), RDN and plasmid were labeled by Cy5.5 and YOYO-1, respectively (Scale bar: 10 μm). Data are presented in the form of mean values ± standard deviation (SD). Source data are provided as a Source Data file.

protein, which has been reported as the no-lysosomal pathway in cells[59]. Rich cellular contents can hinder the intracellular delivery of passively diffusing nanoparticles. The motility of nanoparticles was further observed after entering intracellular. As shown in Supplementary Fig. 27 and Movies 6, 7, in contrast to the "silencing" of Non-RDN@PL, RDN@PL was able to overcome intracellular resistance and moved "happily" due to the high ROS environment in B16F10 cell. As a complement, videos of Cy5.5-labeled particles in living cells were recorded by CLSM, verifying the presence of intracellularly moving nanomotors (Supplementary Fig. 28 and Movies 8, 9). Subsequently, intracellular lysosomal escape ability of RDN@PL was verified by lysosomal co-localization, as illustrated in Fig. 3f and Supplementary Fig. 29a. Non-RDN@PL was partly captured by lysosome after entering cells, which diminished the nanocarrier's subsequent activity and led to disruption of the expression of CRISPR/Cas9 plasmid. The RDN and RDN@PL evaded lysosomal capture through the self-propelling mechanism of intracellular movement and therefore showed noteworthy differences in lysosomal co-localization after 3 h of incubation without compromising their own integrity or that of their cargo plasmids. This outcome is distinguished from the conventional lysosomal escape approach that depends on the proton-sponge effect.

Since tumor cells generate more than 90% of reactive oxygen species during electron transfer in mitochondria[60], the intracellular chemotaxis of RDN@PL was naturally inclined to explore. The co-localization of mitochondria and nanoparticles is displayed in Fig. 3g and Supplementary Fig. 29b. Interestingly, both RDN@PL and RDN exhibited significant mitochondrial secondary targeting effects without being modified with classical targeting molecules. This suggests that mitochondria, the sources of ROS in tumor cells, can effectively induce RDN chemotactic movement and enrichment, providing adequate conditions for subsequent treatment.

The study involved the loading of YOYO-labeled plasmid into Cy5.5-labeled RDN for generating dual fluorescently labeled nanoparticles to evaluate the release ability of RDN@PL in response to tumor cells. The process was illustrated in Fig. 3h. After co-incubation with B16F10 cells for 0.5 h, CLSM was employed to observe the status of the two fluorescent signals within the cells. After 3 h, the green fluorescence indicating the plasmids was markedly distinguished from the red fluorescence indicating the RDN. Furthermore, the Pearson correlation coefficient declined from roughly 0.8 ($t = 0.5$ h) to 0.2 ($t = 3$ h), which was due to the transformation of hemin structure in RDN to become a soluble fragment within the influence of HO-1 expressed exclusively by tumor cells and the release of loaded plasmid occurred alongside the disruption of RDN vesicle structure, the similar phenomenon wasn't observed in HUVECs due to the lack of HO-1 (Fig. 3i). And also, as shown in Supplementary Fig. 30, when HO-1 activity is inhibited by ZnPP in tumor cells[61], RDN@PL clearly had a weak plasmid release, while Non-RDN@PL was unable to release plasmids even in normal B16F10 cells due to the inability to degrade responsively. All the above indicate the excellent safety and responsive targeting effect of RDN@PL on tumor cells.

Gene editing and permeability performance evaluation of nanomotors

The self-driven motion of RDN@PL in the cellular ROS environment resulted in an effective plasmid expression as shown in Fig. 4a, with up to about 2-folds higher GFP fluorescence in tumor cells after incubation with RDN@PL compared to Non-RDN@PL without autonomous moving ability (Fig. 4b). The cell flow cytometry of GFP proteins and western blot analysis of Cas9 proteins further validated these findings (Supplementary Fig. 31). The indel was calculated from the DNA gel electrophoresis bands obtained from the T7E1 assay, and as shown in Fig.4c, after 24 h of co-incubation with the cells, the indel of the RDN-delivered CRISPR/Cas9 system was as high as 43.3 %, while that of the Non-RDN@PL group was only 17.5 %. Sanger sequencing result show successful mutation of LDHA locus (Supplementary Fig. 32), which significantly demonstrates the great advantage of RDN as an active delivery tool for gene editing.

Subsequently, Transwell experiments were further carried out to simulate the transport ability of RDN@PL across the vascular barrier in vitro (Fig. 4d). The release of ROS from tumor cells across the endothelium and the formation of a chemical concentration gradient, which was illustrated and validated by Supplementary Fig. 33, and is expected to drive nanomotors for movement and permeation across the endothelium. As shown in Fig. 4e. the motion group was able to actively cross the endothelium and reach the bottom B16F10 cells, moreover, this active trans endothelial transport ability was significantly inhibited when the ROS scavenger NAC was added to the bottom chamber, demonstrating the significance of the ROS-dependent motility on endothelial penetration. Here, the trans-endothelial mechanism of RDN@PL was further explored (Supplementary Fig. 34). Trans-endothelial penetration of the nanomotor was inhibited by about 50% when HUVECs were treated with caveolin inhibitor, suggesting that RDN@PL across the endothelial layer by caveolin protein-mediated transcytosis driven by the ROS gradient generated by tumor cells.

In addition, HUVECs in the upper chamber after RDN and RDN@PL treatments showed significant activity enhancement, which may be due to the RDN effect with the diffusion of CO released from the tumor cells to promote endothelial cell growth, whereas the activity of the lower B16F10 cells was reduced under this condition, demonstrating the dual effect of RDN@PL to kill tumor cells and activate normal cells (Fig. 4f). Notably, none of the different concentrations of RDN@PL resulted in enhanced viability of HUVECs when treated separately from B16F10 cells (Supplementary Fig. 35), which was attributed to the inability of HUVECs to obtain sufficient CO from RDN due to HO-1 deficiency.

The ROS-dependent self-driven effect was expected to promote the strong penetration of the nanomotor in 3D multicellular tumor sphere (3D MTS) (Fig. 4g). CT26 cells were employed to construct MTS model for validation in vitro. As shown in Fig. 4h, after co-incubation, the distribution of Cy5.5 labeled different samples in MTSs was recorded by CLSM. According to Z-stack (0-120 μm) sections, motile RDN and RDN@PL were induced by ROS to move towards the depth of the MTS and showed a significant tissue penetration advantage. In addition, MTSs pretreated by NAC lost the induction effect of this nanomotor due to ROS deficiency, leading to the inhibition of the strong permeability of RDN@PL, elaborating the ROS dependence of RDN motility. The fluorescence distribution curve in Fig. 4i supports the above conclusion. The strong penetration effect for MTSs led to the high expression of CRISPR/Cas9 system in the cells, as shown in Fig. 4j, the plasmid-expressed green fluorescent protein had a wider distribution in MTSs after RDN@PL treatment of MTSs for 24 h, and further accomplished the efficient cleavage of LDHA locus by CRISPR/Cas9 system (Fig. 4k), and the cutting efficiency about 3-folds that of passive diffusion nanoparticles, which highlights the gene editing advantages of RDN@PL for active delivery in the high-density 3D MTSs model. In addition, the tumor organoid chip was used to evaluate the motility effect of the nanomotor in an in vivo-like physiological environment. As shown in Supplementary Fig. 36, tumor organoid and endothelial cells were planted in the upper and lower channels of the chip, respectively, the particles were added after 8 h of incubation and observed by CLSM. As shown in Supplementary Fig. 36d and Movies 10, 11. RDN@PL underwent significant displacement in the endothelial cell region driven by ROS generated by tumor organoid, a similar phenomenon was not observed in the Non-RDN@PL group. After 6 h incubation, the particles penetrated across the endothelial barrier toward the tumor organoid, and 3D imaging revealed the strong tissue penetration of the nanomotor in the Z-axis direction, which is consistent with previous performance (Supplementary Fig. 36e).

https://doi.org/10.1038/s41467-025-59590-9

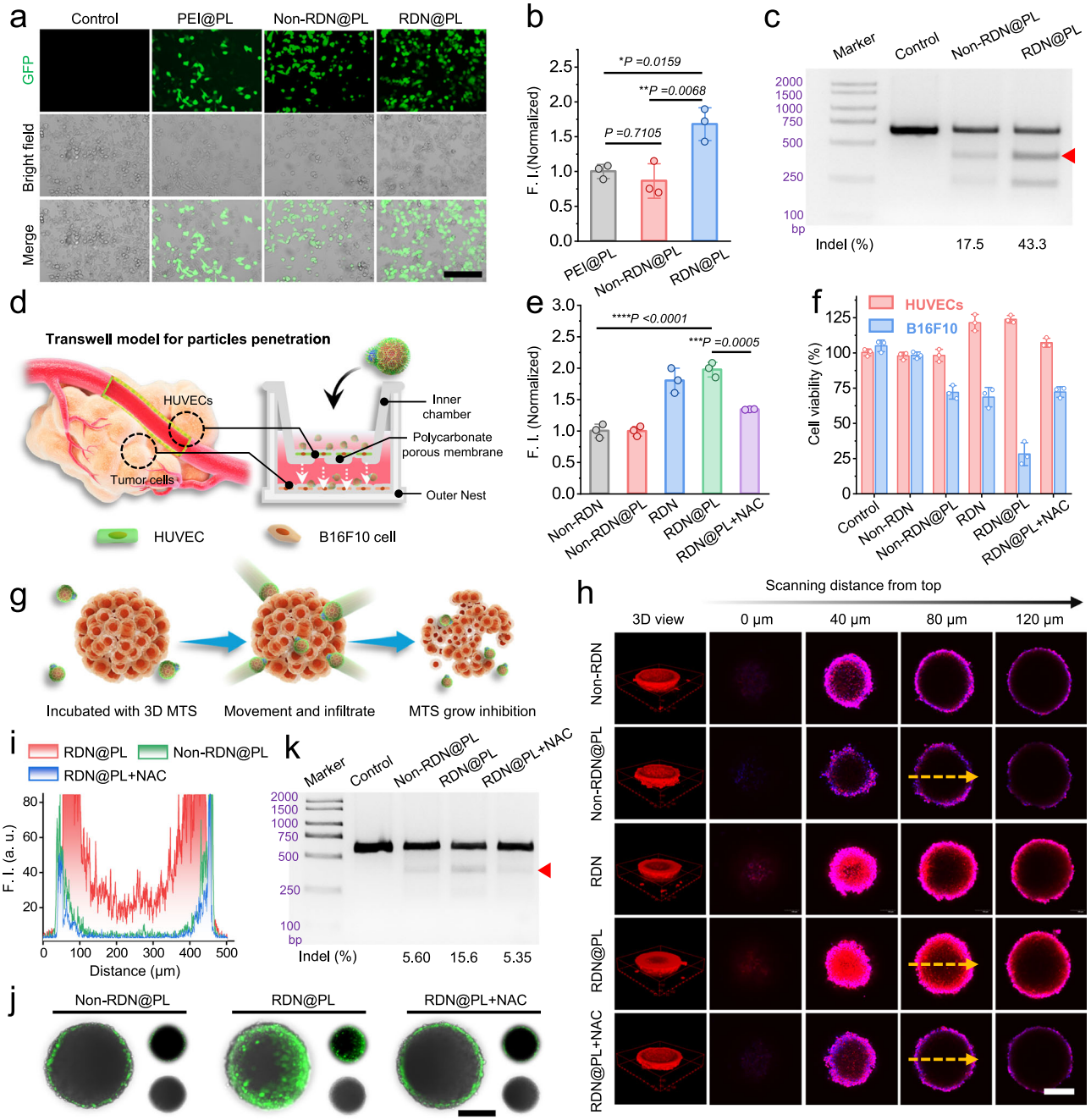

Fig. 4 | Evaluation of gene editing efficiency and therapeutic effect in vitro models of RDN@PL. a The images of GFP green fluorescent protein-expressing of B16F10 cells after transfection by different particles (Scale bar: 200 μm), and the corresponding (**b**) statistical analysis of fluorescence intensity (n = 3 independent experiments). **c** T7E1 indel analysis of B16F10 cells after Non-RDN@PL and RDN@PL mediated transfection of CRISPR/Cas9 plasmid targeting LDHA locus. The experiment was repeated independently three times with similar results, and a representative result is shown. **d** Schematic of the Transwell model in vitro to mimic the tumor vascular barrier, with Cy5.5-labeled particles added in the inner chamber. **e** The statistical analysis of fluorescence intensity in outer nest after particles addition for 12 h (n = 3 independent experiments). **f** The statistical analysis of HUVECs' cellular activity in inner chamber and B16F10 cells in outer nest after 24 h incubation with particles (n = 3 independent experiments). **g** Illustration of the 3D MTSs treatment by RDN@PL. **h** 3D view and Z-stack CLSM images of Cy5.5-labeled particles distributed in MTSs (Scale bar: 200 μm), and corresponding (**i**) Fluorescence distribution curves of Z = 80 μm. **j** The fluorescence images of MTSs transfected with different particles (Scale bar of merge images: 200 μm) The experiment was repeated independently three times with similar results, and a representative result is shown. **k** The frequency of indel mutation determined by T7E1 assay of MTSs with treatment. The experiment was repeated independently three times with similar results, and a representative result is shown.

In vitro and in vivo therapeutic mechanisms investigation of RDN@PL

As a disruptor of the tumor cell electron transport chain, CO impacts mitochondrial metabolic processes and induces ROS production. To ascertain the synergistic therapeutic mechanism of RDN@PL, which is based on CO release and the CRISPR/Cas9 gene editing, the CO scavenger (hemoglobin) was employed to control CO levels, and the treated experimental group was recorded as "CO-". The result of the western blot demonstrated that the CRISPR/Cas9 plasmid was successfully delivered and resulted in effective LDHA protein knockdown (Fig. 5a and Supplementary Fig. 37). To display the changes in intracellular CO levels, CO fluorescent probes were utilized. Additionally,

https://doi.org/10.1038/s41467-025-59590-9

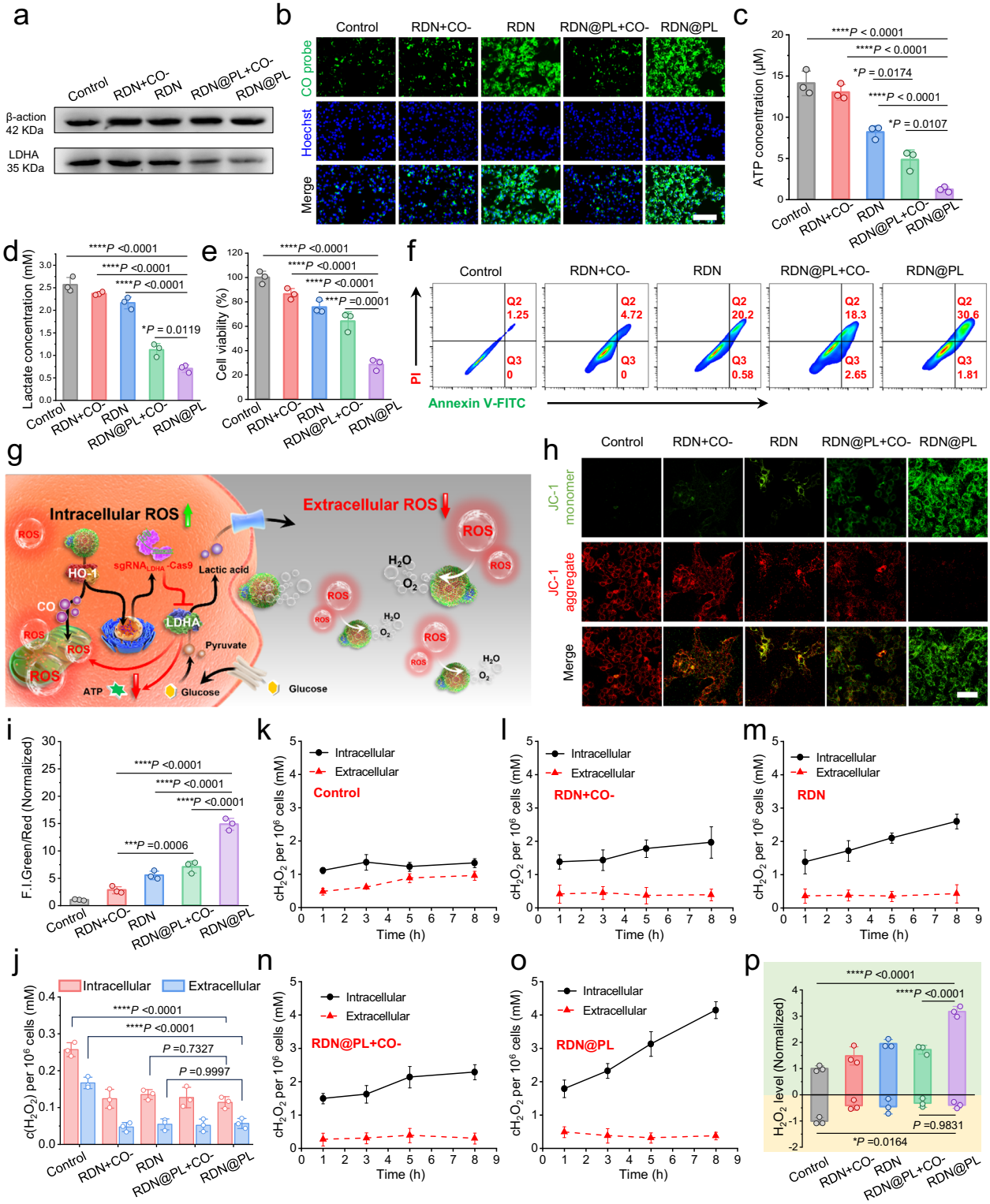

Fig. 5 | Assessment of the RDN@PL's regulation on lactate metabolism and intra/extra-cellular ROS of B16F10 cells. a Western blotting analysis of LDHA after treatment. **b** Fluorescence images of intracellular CO levels after 24 h treatment (Scale bar: 200 μm). Statistical analysis of (**c**) ATP and (**d**) lactate content of B16F10 cells after 24 h treatment ($n = 3$ independent experiments), and (**e**) corresponding cell viability ($n = 3$ independent experiments). **f** Flow-cytometric analysis of the dead and alive staining of B16F10 cells. **g** Illustration of the mechanism that RDN@PL regulates tumor cell metabolism and intra/extra-cellular ROS. **h** The CLSM images of tumor cells mitochondria stained with JC-1 after treatments (Scale bar: 50 μm), and corresponding (**i**) fluorescence ratio analysis ($n = 3$ independent experiments). **j** The inter/external H_2O_2 level of HUVECs after treatments ($n = 3$ independent experiments). **k**–**o** The H_2O_2 level of inter-external of B16F10 cells after treatments with different time ($n = 3$ independent experiments), and the corresponding (**p**) statistical analysis of H_2O_2 level at $t = 8$ h ($n = 3$ independent experiments). Data are presented in the form of mean values ± SD. Significance was assessed via one-way ANOVA with Tukey's post hoc test. Source data are provided as a Source Data file.

both RDN and RDN@PL exhibit high levels of CO release due to the catalytic catabolism of hemin (Fig. 5b and Supplementary Fig. 38). LDHA knockdown notably hinders the glycolytic processes of the tumor cells. Subsequent synergistic action with CO molecules results in the RDN@PL group reducing cellular ATP levels by over 10-folds. Upon examining the lactate content of B16F10 cells for different treatments (Fig. 5d), it is evident that CO alone does not have a significant effect on the lactate content (RDN group). However, once the LDHA was knocked down by CRISPR/Cas9, the extracellular lactate content of B16F10 cells showed a noticeable reduction to 0.7 μM (RDN@PL). Cytotoxicity statistics demonstrate that CO and LDHA knockdown effectively synergized to inhibit the activity of tumor cells. After 24 h, the cell viability reached 28.5% of the control group (Fig. 5e). Flow cytometry apoptosis results indicate that RDN's intracellular CO release can induce late-stage apoptosis in B16F10 cells (Q2 = 20.2). Meanwhile, RDN@PL led to cells late-stage apoptosis for 30.6%, confirming the efficacy of the combined therapy (Fig. 5f).

As elaborated in Fig. 5g, RDN@PL exerted powerful anti-tumor effects through LDHA knockdown and regulation of intra/extra-cellular ROS levels. The mechanism of cellular ROS regulation by this nanomotor was subsequently investigated in detail. As previously stated, RDN@PL has enhanced self-diffusiophoresis due to the catalytic decomposition of ROS outside the cell. Once inside the cell, the released CO and CRISPR/Cas9 plasmid under the influence of HO-1 act on mitochondria and LDHA, respectively, to synergistically intervene in the metabolic processes of tumor cells. JC-1 mitochondrial probe was used to observe the changes in the mitochondrial membrane potential (Fig. 5h). The intensity ratio between green and red fluorescence is a reliable measure of the extent of mitochondrial apoptosis. It is evident that in the RDN group, CO acting only on mitochondria allowed them to maintain most of their activity. However, in the RDN@PL group, when LDHA was knocked down and glycolysis was inhibited, tumor cells compensated for the lack of energy through enhanced mitochondrial aerobic respiration. This intensifies the activity of mitochondria, leading to sensitization of CO action and significant mitochondrial apoptosis (Fig. 5i), which leads to a significant increase in intracellular ROS levels (Supplementary Fig. 39). H_2O_2 concentration was measured to assess the intra/extra-cellular ROS regulatory capacity of RDN@PL, as demonstrated in Fig. 5j. In normal cellular HUVECs, all groups containing RDN were capable of proficiently clearing intra/extra-cellular ROS due to the catalytic activity and long intracellular half-life of RDN. An interesting phenomenon was observed in intra/extra cellular ROS levels of B16F10 cells after treatment, as shown in Figs. 5k–p. The intracellular H_2O_2 content was 2.6 mM per 10^6 cells of RDN group, while it rose to 4.15 mM in RDN@PL group. However, after CO was scavenged (RDN@PL + CO-), the content decreased to 2.29 mM, suggesting the necessity of endogenous CO release in this synergistic strategy. Extracellular levels of ROS decreased by over 50 % in all groups compared to the control, attributed to the substantial amount of extracellular RDN. The transcellular release of ROS was rapidly broken down by extracellular RDN. As a comparison, Non-RDN@PL without ROS catalytic and motile activity, has a weak effect on the regulation of LDHA levels, as well as does not release CO intracellularly, and therefore have no significant regulatory effect on cellular activity, lactate levels, and intra/extra-cellular ROS (Supplementary Fig. 40). It is important to note that the lower extracellular H_2O_2 level measured here is not the true level that drives nanomotor movement. The ROS produced by RDN@PL are immediately cleared by extracellular RDN@PL upon diffusion, while driving its movement. Thus, the reduction in ROS levels and RDN@PL movement occurs simultaneously. To verify this mechanism, we removed the extracellular free particles after RDN@PL was taken up and continued incubation (Supplementary Fig. 41). The results showed that removal of extracellular RDN@PL resulted in a 7-folds increase in H_2O_2 levels when compared to the presence of extracellular particles, which clearly drove the sustained movement of the RDN@PL and promoted cellular uptake. Additionally, the sustained movement of RDN@PL in the cellular environment is shown in Supplementary Fig. 42, where the intracellular nanomotors continuously generate and release ROS, driving the movement of extracellular particles. The diffusion coefficient of the extracellular particles peaked around 8 h. As the cells died due to the therapeutic effect, the movement of the extracellular particles gradually decreased, with significant motion effects lasting for 36 h. Furthermore, the growth status of MTSs after 4 days with different treatments is shown in Supplementary Fig. 43, and RDN@PL demonstrated therapeutic potential in dense 3D tissues.

Tumor cells regulate their microenvironment through multiple pathways like cytokine expression and metabolic reprogramming to create their ecological niche, leading to drug resistance, immunosuppression and other forms of tumor therapy resistance. The disordered tumor vasculature impedes the activation and infiltration of immune cells that require access to the tumor. CO from RDN is thought to promote endothelial cells growth and normalize the tumor vasculature, thereby facilitating the smooth delivery of immune cells and their cargoes (as shown in Fig. 6a). Figure 6b and Supplementary Fig. 44 demonstrate that after 7 days of RDN@PL treatment (The treatment strategy is shown in Fig. 6d). The green fluorescence denoting blood vessels exhibited regularity and homogeneity, which implies a noteworthy elongation of the tumor vasculature and a thickening of the vessel wall after treatment in contrast to the Non-RDN@PL group without CO release. The size of the associated blood vessels on the outside of the tumor also changed significantly after treatment (Supplementary Fig. 45). Furthermore, the non-self-driven Non-RDN@PL encountered challenges when attempting to penetrate solid tumors. Semi-quantitative analysis revealed that the amount of RDN@PL present in solid tumors was approximately 4-5 folds greater than the Non-RDN@PL group (Fig. 6c). This result confirmed the excellent potential of RDN as a delivery vehicle for tumor therapeutics.

Targeting ROS and lactate modulation in tumor cells is expected to deregulate the immune microenvironment and induce the activation of a wide range of immune cells. *C57* mice were treated with different therapeutic agents after subcutaneous tumor modeling (Fig. 6d). As an ICD marker, HMGB1 leaks from tumor cells and stimulates the maturation and chemotaxis of immune cells, such as DCs, after ICD onset. Nevertheless, it is believed that high extracellular ROS levels oxidize HMGB1 and hamper DCs maturation. Here, a combination of Western blot analysis and flow cytometric analysis was used to validate the deregulatory effect of RDN@PL on immune microenvironment inhibition, based on ROS scavenging. The results of Western blot indicated no significant intracellular HMGB1 content change after H_2O_2 treatment (Fig. 6e and Supplementary Fig. 46). However, as indicated in Fig. 6f, due to oxidative failure of HMGB1, the maturation of DCs of H_2O_2 treatment was effectively inhibited (Q2 = 13.0) and were lower than the Control group (Q2 = 18.4). The addition of RDN scavenges extracellular ROS while also generating CO intracellularly, leading to an increased release of HMGB1. This promotes the maturation of DCs and suggests a specific effect of CO in elevating the ICD of tumor cells. After knocking down LDHA (H_2O_2 + RDN@PL), the process of ICD was enhanced, resulting in increased release of HMGB1 and maturation of dendritic cells (DCs). In addition, RDN@PL exhibited a greater proportion of mature DCs with similar levels of HMGB1 release, indicating that scavenging ROS in the tumor microenvironment is highly advantageous for promoting the maturation of DCs.

The CD8+/CD4+ T cell content exhibited a noteworthy advantage in RDN@PL immune activation. Figure 6g demonstrates that active accumulation and CO release of RDN at the tumor site raised the CD8+ T cell content by nearly 3-folds (compared to the Control), whereas LDHA knockdown (RDN@PL group) augmented immunogenicity,

https://doi.org/10.1038/s41467-025-59590-9

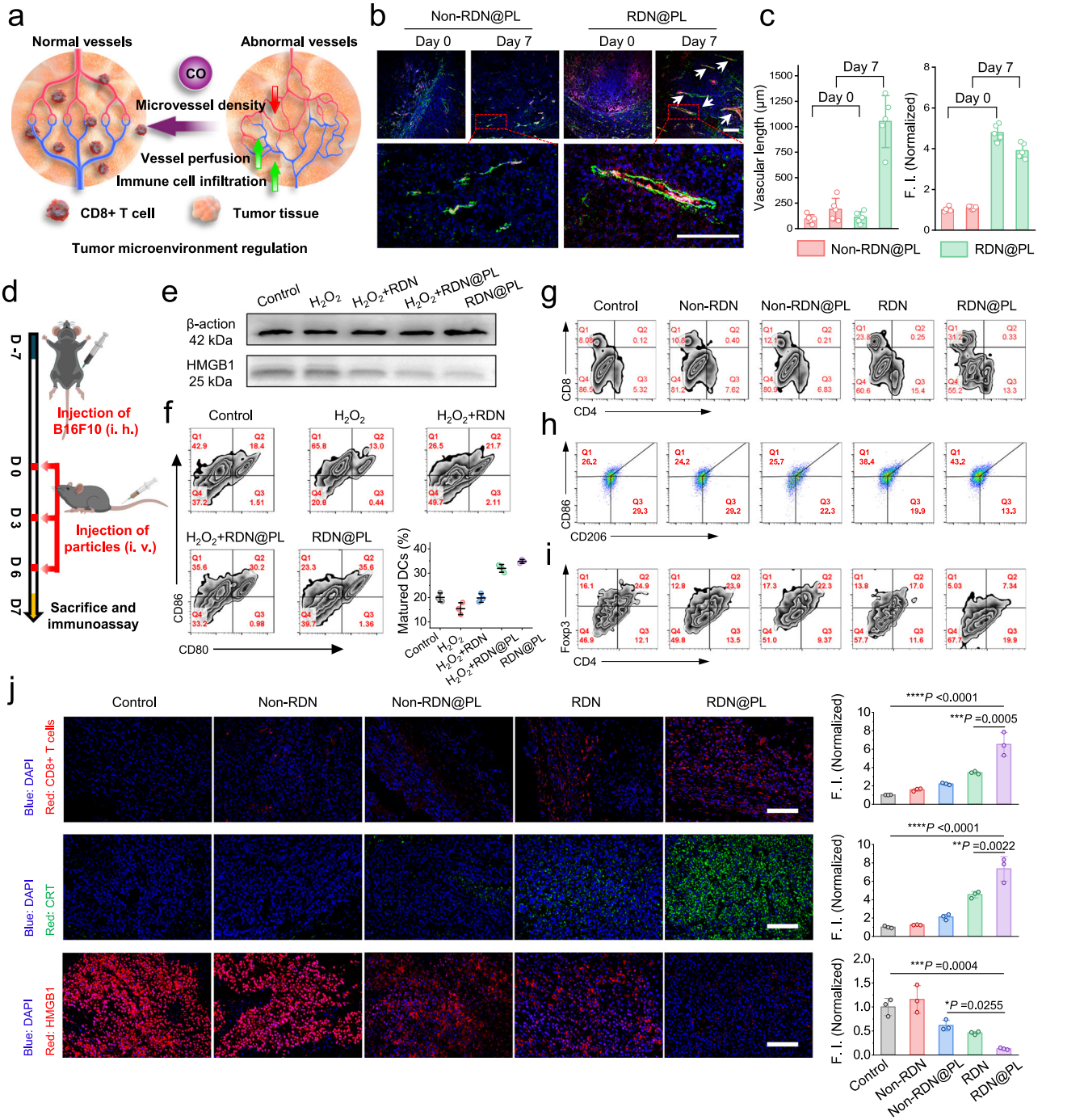

Fig. 6 | In vivo assessment of the effect of RDN@PL on the modulation of the tumor immune microenvironment. a Illustration of the CO modulation on the tumor vascular normalization and immune cell infiltration. **b** Immunofluorescence images of tumor tissues after 7 days of treatment, green: α-SMA, red: Cy5.5-labeled particles, blue: nucleus (Scale bar: 200 μm). Corresponding (**c**) Statistical analysis of vessel length (Left, n = 5 independent experiments) and Cy5.5 fluorescence intensity (Right, n = 5 independent experiments). **d** The treatment schematic for the efficacy validation of vascular normalization and immunoassay. **e** Western blotting analysis of HMGB1 after treatment (2 % H_2O_2 for in situ tumor injection to create a high oxidative environment), and corresponding (**f**) Flow-cytometric analysis of DCs in spleen (Q2 area represents the ratio of mature DCs) and corresponding statistical analysis (n = 3 independent experiments). Flow-cytometric analysis of (**g**) T cells, (**h**) macrophage cells and (**i**) Treg cells of tumor tissues from *C57* mice after different treatments. **j** Immunofluorescence images of CD8+ T cells, CRT, and HMGB1 of tumor tissues with different treatments (Scale bar: 200 μm) and corresponding statistical analysis of fluorescence intensity (n = 3 independent experiments). Data are presented in the form of mean values ± SD. Significance was assessed via one-way ANOVA with Tukey's post hoc test. Source data are provided as a Source Data file.

thereby resulting in increased CD8+ T cells (Q1 = 31.2). Furthermore, the RDN had an ICD-inducing effect that caused a reduction in the M2 polarization of TAM (as shown in Fig. 6h) and led to an increase in M1-type TAM. The LDHA knockdown (RDN@PL group) had a further effect of polarizing M2 towards M1 by decreasing the lactate content, thereby promoting tumor resistance of TAM, which has been previously reported[62,63]. Additionally, Treg cells content decreased after RDN treatment (Q2 = 17.0) as a suppressor cell of the tumor's immune program, which could be attributed to the enhanced ICD effect. Furthermore, due to the reliance on lactate for energy, Treg

cells exhibited further decrease (Q2 = 7.34) following knockdown of LDHA (in the RDN@PL group).

Tumors from mice were excised and underwent immunohistochemical analysis after treatment. The findings are presented in Fig. 6j. Enhanced ICD was induced by increasing intracellular ROS and extracellular ROS scavenging capacity of RDN. This caused a noteworthy rise in the marker CRT, situated at the outer side of the tumor cell membrane and the subsequent extracellular release of HMGB1. This effect was evidenced by an increase and a decrease in fluorescent labeling of the tissue sections, respectively. Due to the normalization of tumor vasculature and the Immune Cell Death (ICD) enhancement effect, CD8+ T-cell infiltration in solid tumor tissues was significantly increased in the RDN@PL group. Further, the distal tumor model was constructed to assess the activation of systemic immunity by RDN@PL (Supplementary Fig. 47). After treatment of the primary tumors, the CD8+ T cell levels of both tumors were significantly elevated compared to the Control, and the tumor volume was suppressed simultaneously. All the above prove that RDN@PL, as a self-driven gene editing delivery system, has excellent potential in regulating tumor metabolism and the immune microenvironment.

Therapeutic efficacy validation of RDN@PL on solid tumor model

In vivo investigations were conducted on *C57* mice to substantiate the tumor effectiveness of RDN@PL. The biodistribution and tumor targeting effects of particles were first assessed by IVIS spectrum. As shown in Supplementary Fig. 48, RDN@PL demonstrated intra-tumor distribution 0.5 h after the first injection, and intra-tumor particle abundance reached a maximum after 12 h, while Non-RDN@PL showed slower tumor enrichment, implying that RDN@PL acts as a self-driven nanomotor with significantly improved tumor delivery efficiency. In vivo treatment was subsequently carried out, after 7 days of subcutaneous modeling with 4 administrations via the tail vein (Fig. 7a), the tumor volume in the control group grew to 1906 mm^3 within 14 days, as shown in Fig. 7b. The passively spreading Non-RDN@PL treatment resulted in a slight reduction of tumor volume (1378 mm^3) compared to the non-significantly efficacious Non-RDN group (1713 mm^3), demonstrating the effective effect of LDHA knockdown on tumor growth inhibition. Due to the synergistic enhancement of intracellular and extracellular apoptosis and ICD, the RDN group effectively inhibited tumor growth. The tumor volume reached only 461 mm^3 after treatment, thus verifying the efficacy of RDN in active delivery targeting the tumor microenvironment. After loading the gene editing plasmid, the RDN@PL group's multilevel synergistic strategy for regulating the tumor immune microenvironment led to optimal tumor suppression. After two doses, a significant reduction in tumor volume was observed, and it reached 115 mm^3 ultimately. Tumor removal images and weights are presented in Fig. 7c, and the significant reduction in size and weight was observed after RDN@PL treatment, indicating the effectiveness of this therapeutic strategy against tumor growth. The biodistribution status of RDN@PL after treatment is shown in Supplementary Fig. 49, the enrichment level in tumor reached 1.81 mg per 100 mg tissue, and the excess components were mainly metabolized in the liver. Furthermore, the significant weight drops and organ toxicity of mice weren't observed during treatment, demonstrating the excellent biosafety of RDN@PL (Fig. 7d and Supplementary Fig. 50). The survival curves of mice after different treatments are shown in Fig. 7e, where RDN@PL-treated mice demonstrated a 90 % survival rate after 60 days, showing the great potential of this nanomotor to treat tumors through metabolic and immune modulation.

T7E1 assay was employed to assess tumor gene editing efficiency after treatment, as presented in Fig. 7f. RDN@PL demonstrated a 2-folds higher indel value than Non-RDN@PL, owing to the ROS chemotaxis as well as solid tumor penetration of the autonomous vector RDN. Specifically, the RDN@PL vector's ROS chemotaxis allowed for better targeting of the tumor microenvironment, while also possessing gene-editing capability that is HO-1 responsive. The gene editing ability of RDN@PL was found to be tumor-responsive, as demonstrated by the absence of cleavage fragments of LDHA locus in liver, which serves as a metabolic scavenging organ. Due to the LDHA knockdown, the tumor cells treated with plasmid-containing nanocarriers exhibited considerable LDHA down-regulation, which was notably more pronounced with RDN@PL, and showed a significant advantage over the other groups after both the first and four injections (Fig. 7g and Supplementary Fig. 51), thereby confirming the efficacy of RDN as a delivery platform for active gene editing. To validate the proportions of apoptotic, proliferative, and necrotic areas in the various treatment groups, Tunel, Ki67, and H&E immunohistochemistry experiments were conducted (Fig. 7i). The quantitative analysis in Fig. 7j revealed that tumors treated with RDN@PL had the highest apoptosis (76.4%) and necrotic area (38.9%). Moreover, the proportion of Ki67-positive cells (32.9 %) was significantly suppressed, indicating the decreased proliferation of tumor cells. In addition, the CRISPR/Cas9 plasmid of scramble sgRNA was loaded on RDN to assess the targeting of the LDHA-target sgRNA sequence design in a controlled manner (Supplementary Fig. 52). Under the same treatment process, scrambled sgRNA didn't show any gene editing effect of LDHA, and off-target analysis also showed that LDHA-target sgRNA had no significant cleavage effect on similar DNA sequences. Tumor growth curves, Tunel and LDHA immunofluorescence results further highlight the clear advantage of LDHA-target sgRNA after plasmid delivery, which further confirmed the better tumor-targeting capability and biosafety of RDN@PL. These findings suggest that RDN@PL holds promising therapeutic potential for solid tumors as a delivery system for gene editing, which effectively regulates tumor metabolism and microenvironment at multiple levels.

Discussion

Here, we synthesized a form-effect integrated dual Janus gene-editable nanomotor through self-assembly and phase separation. The RDN@PL exhibited excellent self-propulsion by utilizing extracellular ROS from tumor cells as fuel. In addition, RDN@PL exhibited microbial-like chemotaxis. Inside a Y-shaped microfluidic channel, it showed remarkable tumor cell-directed motility. By exploiting the high ROS microenvironment in tumors, the nanomotor can move towards tumor cells for effective targeted transport chemotactically and cellular uptake (approximately 2.5-folds greater than passive diffusion particles). The self-propelled capability of RDN@PL facilitated highly effective 3D multicellular tumor sphere penetration, with a penetration depth of 73.5 μm. The RDN@PL, which was loaded with the CRISPR/Cas9 plasmid was able to precisely penetrate the tumor cells and release the plasmids for gene editing in response to HO-1 overexpression in the cells. The self-driven capability of RDN@PL resulted in a significantly higher gene-editing efficiency (13.3 %) for solid tumors, which was about 2.1 folds greater than that of the passive-diffusion particles.

In addition, we proposed a tumor metabolic intervention and enhanced immunotherapy strategy through intra/extra-cellular Janus-synergy and grading regulation. RDN@PL was uptake by tumor cells through chemotactic targeting and dissociated by overexpressed HO-1, releasing of CO and loaded plasmids, responsively. By knocking out the LDHA with Cas9 gene editing, the cellular ATP reduced to 2.92 μM (13.9 μM in Control group), led to the mitochondrial compensatory metabolism and combined CO cause the intracellular ROS storm, and result in an intensification of the ICD of tumor cells. The increase in HMGB1 release was 7.2-fold compared to the Control. Meanwhile, the extracellular depletion of ROS by RDN@PL (not taken up by cells) reversed the ICD inhibition caused by HMGB1 oxidation in the tumor's high-ROS microenvironment, leading to the activation of DCs and a series of immune cells, which

https://doi.org/10.1038/s41467-025-59590-9

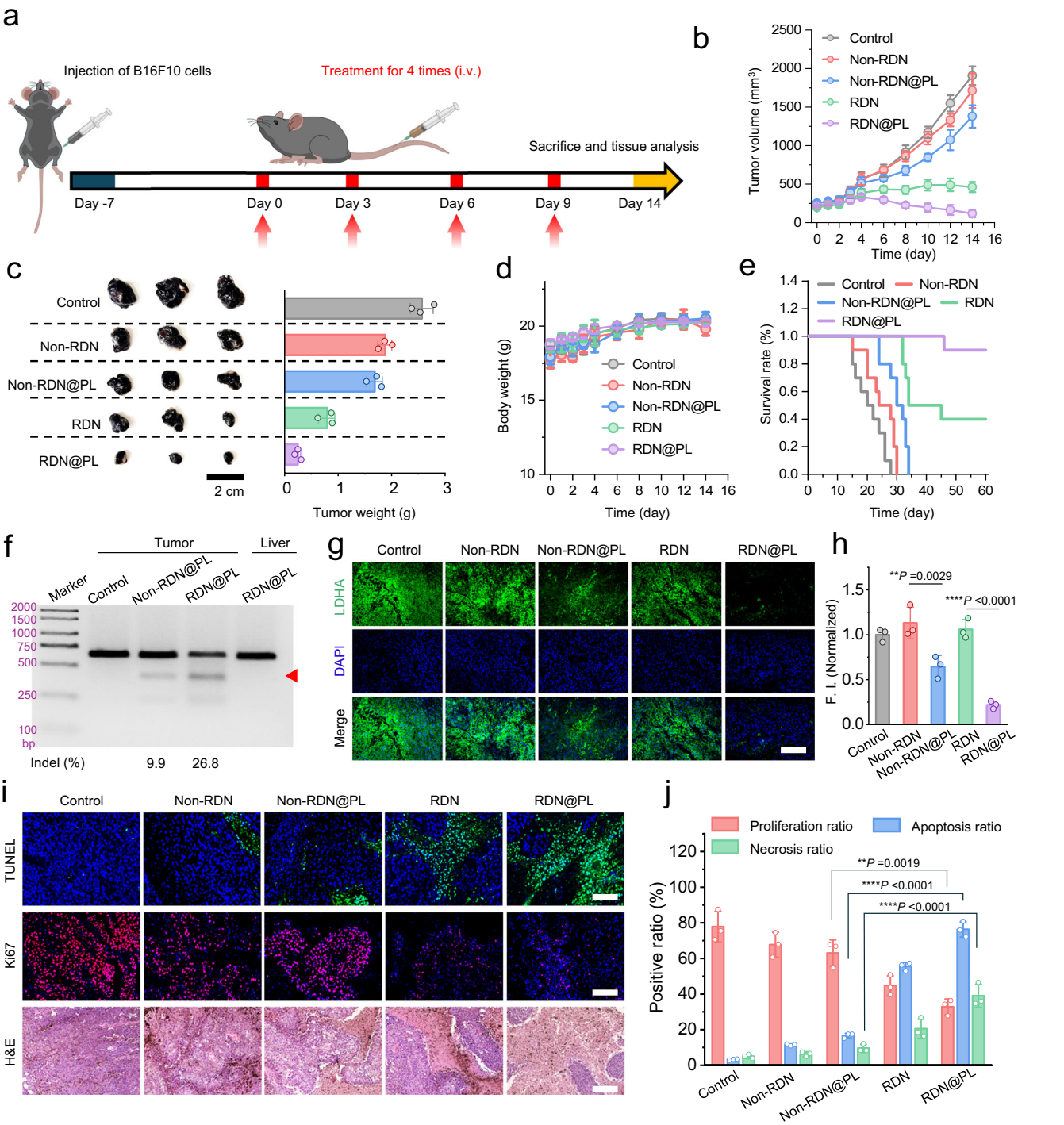

Fig. 7 | In vivo efficacy evaluation of RDN@PL for malignant melanoma solid tumors. a Schematic illustration of *C57* mice subcutaneous melanoma model. **b** Tumor volume curves during treatment (n = 3 mice). **c** The image and tumor weight statistic of dissected tumors (n = 3 mice). **d** Body weights curves (n = 3 mice) and (**e**) Survival rate of mice with different treatment (n = 10 mice). **f** Frequency of indel mutation detected by T7E1 assay of tumor and liver after treatment. **g** The immunofluorescence images of LDHA in tumor with different treatments (Scale bar: 200 μm), and corresponding (**h**) Statistical analysis of fluorescence intensity (n = 3 independent experiments). **i** H&E, TUNEL and Ki-67 immunofluorescence staining images of tumor tissue sections after treatments (Scale bar: 100 μm), and corresponding (**j**) Statistical analysis of tumor cell proliferation, apoptosis and tumor tissue necrosis area ratio (n = 3 independent experiments). Data are presented in the form of mean values ± SD. Significance was assessed via one-way ANOVA with Tukey's post hoc test. Source data are provided as a Source Data file.

synergized with the tumor vasculature-normalizing effect of CO and resulted in a significant infiltration by CD8+ T cells. The Janus modulation of tumor intra/extracellular ROS levels demonstrated effective tumor suppression. In addition, gene-level knockdown of LDHA resulted in decreased lactate levels, which in turn downregulated Treg cells and M2 macrophages to eliminate the immunosuppressive environment of tumor.

In summary, RDN@PL achieves precise targeting and potent penetration into tumor tissues through ROS-dependent self-driven action and performs responsive gene editing catalyzed by

overexpression enzymes in tumor cells, while having no apparent effect on normal cell tissues. Comparing relevant studies in recent years, the self-driven delivery strategy of this dual Janus gene-editable nanomotor, the oppsing regulation of the inter/external environment of tumor cells, and the therapeutic mechanism of tumor metabolic perturbation and microenvironmental regulation at the gene level provide a paradigm for tumor treatment (Supplementary Table 2).

Methods

Regulatory

All animal studies were approved (Approval No. IACUC-2306013) by the Institutional Animal Care and Use Committee (IACUC) of the Animal Experiment Center of Nanjing University (Nanjing, China). All animal experiments were performed in accordance with the Regulations for the Administration of Affairs Concerning Experimental Animals approved by the State Council of People's Republic of China.

Materials

The main chemical reagents used for synthesis were all purchased from as follows: Hemin (Sigma-Aldrich, Catalog no. 3741), Chitosan (Shanghai yuanye Bio-Technology Co., Ltd, Catalog no.S31060), Protoporphyrin (Sigma-Aldrich, Catalog no. P8293), 1-(3-Dimethylaminopropyl)-3-ethylcarbodiimide (EDC, Sigma-Aldrich, Catalog no. E7750), N-Hydroxysuccinimide (NHS, Sigma-Aldrich, Catalog no. 130672). Antibodies for western blot analysis were used as follows: HMGB1 Monoclonal antibody (Catalog no. AG2167, lgG), LDHA Polyclonal antibody (Catalog no. AF0216, lgG) were purchased from Beyotime Biotechnology (China). All antibodies for flow cytometry analysis were used from BioLegend (USA): APC anti-mouse CD3e (Catalog no.100311), FITC anti-mouse CD4 (Catalog no.100509), PE anti-mouse CD8a (Catalog no.100707), APC anti-mouse CD11c (Catalog no.117309), FITC anti-mouse CD80 (Catalog no.104705), PE anti-mouse CD86 (Catalog no.105007), PE anti-mouse FOXP3 (Catalog no.126404), FITC anti-mouse CD4 (Catalog no.100509), APC anti-mouse F4/80 (Catalog no.123115), PE/Cyanine7 anti-mouse/human CD11b (Catalog no.101215), Brilliant Violet 421™ anti-mouse CD206 (Catalog no.141717). T7 endonuclease I (T7E1) enzyme was purchased from Vazyme. Trypsin–EDTA digest was purchased from BioChannel Biological Technology Co., Ltd (China). Serum-free cell freezing medium cell (CELLSAVING, Catalog no.C40100) was obtained from New Cell & Molecular Biotech (China). Fetal bovine serum (FBS) was purchased from ExCell Bio (China). D-Luciferin Firefly, Free Acid D, Propidium iodide (PI), and Calcein AM dye were obtained from Yeasen Biotechnology Co., Ltd. (Shanghai, China). Cell Counting Kit-8 (CCK-8) was purchased from TargetMol Chemicals Inc. (USA). The cell culture dishes and transwell cell chambers were obtained from NEST Biotechnology Co. Ltd. (Wuxi, China).

Cell lines and mice

B16F10, CT26, Raw264.7 and HUVEC cell lines were purchased from Cell Resource Center, Peking Union Medical College (PCRC). All cell lines were cultured in DMEM (KeyGEN BioTECH) supplemented with 10% fetal bovine serum (ExCell Bio), 100 U mL^{-1} of penicillin G sodium and 100 μg mL^{-1} of streptomycin sulfate in a humidified atmosphere that contained 5% CO_2 at 37 °C. All cell lines were negative by mycoplasma testing. C57BL/6J mice (6–8 weeks, 18–20 g, female) were purchased from Jiangsu Wukong Biotechnology Co., Ltd. All animals were bred in a pathogen-free facility with a 12 h light/dark cycle at 20 ± 3 °C and 40–50% humidity and had ad libitum access to food and water.

Characterizations

The morphology of nanoparticles was detected by TEM (JEM-200CX; JEOL Ltd.). The UV-visible spectra were carried out on a microplate photometer (Multiskan FC; Thermo Fisher Scientific Inc.). Zeta potentials of all samples were detected by electrophoretic light scattering (Brookhaven Instruments Corporation, Holtsville, NY, USA). FTIR spectrum was recorded by an FTIR spectrometer (NEXUS870; Nicolet). Fe content and biodistribution was determined and calculated by Inductively coupled plasma (ICP) (IRIS Intrepid II; Thermo Fisher Scientific Inc.). Flow cytometry data were acquired on a flow cytometer (BD Biosciences) and analyzed using FlowJo software. Particle trajectory tracking and velocity analysis were carried out by Fiji software.

Synthesis of chitosan-hemin (Cs-He) and chitosan-protoporphyrin (Cs-Pp)

Chitosan-hemin amphiphilic molecules were obtained by a typical EDC/NHS reaction. Briefly, 13.04 mg (0.02 mmol) of hemin was dissolved in 5 mL of DMSO by sonication for 5 min, followed by the addition of 47.2 mg (0.24 mmol) of EDC, and the mixture was stirred at 37 °C for 20 min, followed by the addition of 6.9 mg (0.06 mmol) of NHS, and stirred for 30 min, and then 40 mg of chitosan, the reaction was stirred overnight under N_2 atmosphere. The mixture was purified by dialysis using a dialysis bag with M_D = 3000 Da for 3 days, and the resulting product was lyophilized and stored at 4 °C for later use.

The synthesis of Cs-Pp followed a similar approach, 11.25 mg (0.02 mmol) of protoporphyrin was dissolved in 5 mL of DMSO by sonication for 5 min, and the following steps were consistent with the synthesis of Cs-He.

Synthesis of chitosan-palmitic acid (Cs-Pa)

Cs-Pa amphiphilic molecules were prepared by a method similar to the previous step. Briefly, 5.13 mg (0.02 mmol) palmitic acid was dissolved in 5 mL of DMSO by sonication, followed by the addition of 47.2 mg (0.24 mmol) of EDC, and the mixture was stirred at 37 °C for 20 min to activate the carboxyl group in the palmitic acid. 6.9 mg (0.06 mmol) NHS was added immediately after the above mixture. 6.9 mg (0.06 mmol) NHS was added to the above mixture and stirred for 30 min. 40 mg Chitosan was added subsequently and the mixture was stirred overnight under N_2 atmosphere. The mixture was purified by dialysis using a dialysis bag with M_D = 3000 Da and the resulting product was lyophilized and stored at 4 °C.

Preparation of ROS-driven nanomotor (RDN) and Non-RDN

RDN was prepared by a typical hydrated film method. Briefly, 40.9 mg Cs-He were dispersed with 9.1 mg Pa-Cs in a flask using 10 mL of chloroform solution, and the mixture was sonicated at 25 Hz for 10 min to mix thoroughly. The mixture was then transferred to an oven at 60 °C for overnight drying to allow complete volatilization of the solvent to form a film of the mixture. Subsequently, 10 mL PBS was added to the flask and moistened the mixture film, and the mixture solution was sonicated and hydrated for 60 min at 45 Hz to form hybrid vesicles. 11,000 × *g* centrifugation for 15 min was used to collect the above hybrid vesicles, and Janus RDN was obtained by standing for 72 h at 37 °C. The synthesis of Non-RDN followed a similar approach, using Cs-Pp to replace Cs-Hemin in order to prepare Non-RDN without ROS consumption, motility and CO release ability.

Preparation of RDN@PL and Non-RDN@PL

Electroporation was used to allow the entrapment of Cas9/sg-LDHA plasmid of the RDN and Non-RDN. In brief, RDN with different mass ratios were mixed and dispersed with plasmids in PBS, and then transferred to an electroporation cup for encapsulation (Gemini X2, BTX Harvard Bioscience). The optimal setting used for the electroporation was 10 pulses at 2500 V. After electroporation, the mixture was transferred to a centrifuge tube and stood overnight for nanostructure recovery and further electrostatic adsorption of the plasmid. The unloaded free plasmid was detected by agarose gel electrophoresis, and the encapsulation and loading efficiency of RDN on the

plasmid were calculated. Finally, RDN@PL were separated by 11,000 ×g centrifugation for 15 min. The preparation of Non-RDN@PL followed a similar approach.

Analysis of the motion behaviors of the particles

The videos taken by EVOS FL Auto Cell Imaging System (EVOS FL AUTO, Thermo Fisher Scientific Inc.) were analyzed using the Manul Track plugin for Fiji software to record coordinates for each particle. The mean-square-displacement (MSD) of the particles was calculated by using the formula of MSD $(\Delta t) = (xi_{(t+\Delta t)}\text{-}xi_{(t)})^2$, where x is a two-dimensional vector, i is an index to show x and y, and Δt represents the time interval. and the D_{eff} was obtained by fitting the MSD data to MSD $_{(\Delta t)} = 4D_{eff}\,\Delta t$. In all cases, at least 15 particles were analyzed.

T7E1 assay

To acquire genomic DNA, the transfected cells and tissues were collected. PCR was used to amplify the genomic area around the Cas9 target site with primers CAAAGCGAGGGTCTGAACGG and CCCACCACCTGGCCAAAGTATTAT, which was subsequently purified using the TIANquick Midi Quantification Kit (TIANGEN BIOTECH, China). The T7E1 assay required a total of 200 ng purified PCR products. The products were separated on a 1 % agarose gel and photographed using a gel documentation system. ImageJ computed indel percentage. The primer sequences used for off-target experiments are provided in the Supplementary Information.

Detection of Intracellular ROS

The generation of ROS was determined by the ROS-sensitive probe DCFH-DA. After inoculation in a 24-well plate and overnight culture, B16F10 cells were incubated in DMEM for 24 h with different nanoparticles (100 μg mL^{-1}). DCFH-DA in fresh medium (10 μM) was used to further incubate the cells for 30 min at 37 °C. After removing the medium, the cells were washed twice with PBS and observed by a fluorescence microscope.

Lactate content assay

B16F10 cells (5×10^5 cells mL^{-1}, 2 mL) were inoculated in 6-well plates and incubated overnight for 12 h. Blank medium, RDN, RDN + CO-, RDN@PL + CO-, and RDN@PL (200 μg mL^{-1}) were then added to the corresponding wells and incubated for 24 h. The medium was collected and the cells were gently washed with PBS, and all removed fluid was mixed for the next step. 200 μL of RIPA lysate was added to each well, incubated for 10 min. All wash buffer was collected for the next step of analysis. The supernatant was mixed with cell lysate and wash buffer, and the lactate content of the different groups was determined using a lactate kit (Nanjing Jiancheng Institute of Biological Engineering).

Intra/extra-cellular H_2O_2 content assay

B16F10 cells (5×10^5 cells mL^{-1}, 2 mL) were inoculated in 6-well plates and incubated overnight for 12 h. Blank medium, RDN, RDN + CO-, RDN@PL + CO-, and RDN@PL (100 μg mL^{-1}) were then added to the corresponding wells and pre-incubated for 24 h. Subsequently, discarded the old supernatant and carefully washed with PBS. Re-added the corresponding particles (200 μg mL^{-1}) and continue incubation for 1, 3, 5, and 8 hours, respectively. The medium was collected and the cells were gently washed with PBS, and all removed fluid was mixed for the next step. 100 μL of trypsin digest was added to each well, incubated for 1 min, then centrifuged at 90 g for 10 min and the bottom cells were collected. All wash buffer was collected for the next step of analysis. The lower cells were digested by 100 μL trypsin for 1 min and 100 μL culture solution was used to terminate the digestion. The cells were then centrifuged, the supernatant removed and the cell sediment left. The cell sediment was washed with 200 μL PBS, centrifuged, the supernatant removed and the cell sediment left. Subsequently, 250 μL of cell lysate was added to fully lyse the obtained cells for 15 min, centrifuged at 800 × g for 10 min, and the supernatant was taken and the intracellular lactate content of the different groups was determined using hydrogen peroxide test kit (Beijing Solarbio Science & Technology Co., Ltd.).

Statistics and reproducibility

Data analysis was conducted using the software Microsoft Office Excel and PowerPoint 365, Origin 2021 pro, and Image J software. Flow cytometry were analyzed on Flowjo-V10 software. Living image 4.4 software was used to analyze IVIS data. The statistical analysis was performed using SPSS Statistics software. Significant differences between different groups was analyzed by one-way analysis of variance (ANOVA) and Tukey's post hoc test. The criterion was expressed as $^*P < 0.05$, $^{**}P < 0.01$, $^{***}P < 0.001$, $^{****}P < 0.0001$, and $P > 0.05$ represents non-significant difference (n. s.).

Reporting summary

Further information on research design is available in the Nature Portfolio Reporting Summary linked to this article.

Data availability

The source data generated in this study are provided in the Supplementary Information/Source Data file. The full image dataset is available from the corresponding author upon request. Source data is available for Figs. 2–7 and Supplementary Figs. 2, 5, 6, 8, 9, 11, 13, 14, 16, 18, 19, 21, 23, 24, 26, 30, 33-35, 38, 40-43, 47, 49, 51, 52 in the associated source data file. Source data are provided with this paper.

References

1. Rosenblum, D. et al. CRISPR-Cas9 genome editing using targeted lipid nanoparticles for cancer therapy. *Sci. Adv.* **6**, eabc9450 (2020).
2. Lebek, S. et al. Ablation of CaMKIIδ oxidation by CRISPR-Cas9 base editing as a therapy for cardiac disease. *Science* **379**, 179–185 (2023).
3. Li, T. et al. CRISPR/Cas9 therapeutics: progress and prospects. *Signal Transduct. Tar.* **8**, 36 (2023).
4. Ryu, N. et al. Effective PEI-mediated delivery of CRISPR-Cas9 complex for targeted gene therapy. *Nanomed. Nanotechnol.* **14**, 2095–2102 (2018).
5. Glass, Z., Li, Y. & Xu, Q. Nanoparticles for CRISPR–Cas9 delivery. *Nat. Biomed. Eng.* **1**, 854–855 (2017).
6. Li, B. et al. Combinatorial design of nanoparticles for pulmonary mRNA delivery and genome editing. *Nat. Biotechnol.* **41**, 1410–1415 (2023).
7. Zhang, L. et al. Triple targeting delivery of CRISRP/Cas9 to reduce the risk of cardiovascular diseases. *Angew. Chem. Int. Ed.* **58**, 12404–12408 (2019).
8. Pan, Y. et al. Near-infrared upconversion–activated CRISPR-Cas9 system: a remote-controlled gene editing platform. *Sci. Adv.* **5**, eaav7199 (2019).
9. Chen, X. et al. Non-invasive activation of intratumoural gene editing for improved adoptive T-cell therapy in solid tumours. *Nat. Nanotechnol.* **18**, 933–944 (2023).
10. Yan, X., Pan, Q., Xin, H., Chen, Y. & Ping, Y. Genome-editing prodrug: targeted delivery and conditional stabilization of CRISPR-Cas9 for precision therapy of inflammatory disease. *Sci. Adv.* **7**, eabj0624 (2021).
11. Nelson, B. & Pané, S. Delivering drugs with microrobots. *Science* **382**, 1120–1122 (2023).
12. Wan, M., Li, T., Chen, H., Mao, C. & Shen, J. Biosafety, functionalities and applications of biomedical micro/nanomotors. *Angew. Chem. Int. Ed.* **60**, 13158–13176 (2020).

13. Li, H. et al. Medical micro- and nanomotors in the body. *Acta Pharm. Sin. B* **13**, 517–541 (2022).
14. Wang, Y. et al. NIR-II light powered asymmetric hydrogel nanomotors for enhanced immunochemotherapy. *Angew. Chem. Int. Ed.* **62**, e202212866 (2022).
15. Pan, T. et al. Bio-micromotor tweezers for noninvasive bio-cargo delivery and precise therapy. *Adv. Funct. Mater.* **32**, 2111038 (2022).
16. Kagan, D. et al. Acoustic droplet vaporization and propulsion of perfluorocarbon-loaded microbullets for targeted tissue penetration and deformation. *Angew. Chem. Int. Ed.* **124**, 7637–7640 (2012).
17. Xi, W. et al. Rolled-up magnetic microdrillers: towards remotely controlled minimally invasive surgery. *Nanoscale* **5**, 1294–1297 (2012).
18. Chen, W. et al. Recent progress of micro/nanorobots for cell delivery and manipulation. *Adv. Funct. Mater.* **32**, 2110625 (2022).
19. Changyong, G. et al. Biomedical micro-/nanomotors: from overcoming biological barriers to in vivo imaging. *Adv. Mater.* **33**, 2000512 (2020).
20. Wang, Y. et al. Photocatalytically powered "Match-Like" nanomotor for light-guided active SERS sensing. *Angew. Chem. Int. Ed.* **57**, 13110–13113 (2018).
21. Wang, Y. et al. Magnetic nanorobots as maneuverable immunoassay probes for automated and efficient enzyme linked immunosorbent assay. *ACS Nano* **16**, 180–191 (2022).
22. Wang, S.-H. et al. Hydrogen-powered microswimmers for precise and active hydrogen therapy towards acute ischemic stroke. *Adv. Funct. Mater.* **31**, 2009475 (2021).
23. Yang, M. et al. Swarming magnetic nanorobots bio-interfaced by heparinoid-polymer brushes for in *vivo* safe synergistic thrombolysis. *Sci. Adv.* **9**, eadk7251 (2023).
24. Zhang, H. et al. Dual-responsive biohybrid neutrobots for active target delivery. *Sci. Robot.* **6**, eaaz9519 (2021).
25. Chen, H. et al. A nitric-oxide driven chemotactic nanomotor for enhanced immunotherapy of glioblastoma. *Nat. Commun.* **14**, 941 (2023).
26. Li, T. et al. A universal chemotactic targeted delivery strategy for inflammatory diseases. *Adv. Mater.* **34**, 2206654 (2022).
27. Ye, Y. et al. Apoptotic tumor dna activated nanomotor chemotaxis. *Nano Lett.* **21**, 8086–8094 (2021).
28. Liu, Z. et al. GSH-induced chemotaxis nanomotors for cancer treatment by ferroptosis strategy. *Sci. China Chem.* **65**, 989–1002 (2022).
29. Chao, Y. & Liu, Z. Biomaterials tools to modulate the tumour microenvironment in immunotherapy. *Nat. Rev. Bioeng.* **1**, 125–138 (2023).
30. Cheung, E. & Vousden, K. The role of ROS in tumour development and progression. *Nat. Rev. Cancer* **22**, 280–297 (2022).
31. Rabinowitz, J. & Enerbäck, S. Lactate: the ugly duckling of energy metabolism. *Nat. Metab.* **2**, 566–571 (2020).
32. Zhang, D. et al. Metabolic regulation of gene expression by histone lactylation. *Nature* **574**, 575–580 (2019).
33. Watson, M. et al. Metabolic support of tumour-infiltrating regulatory T cells by lactic acid. *Nature* **591**, 645–651 (2021).
34. Ding, B. et al. Sodium bicarbonate nanoparticles for amplified cancer immunotherapy by inducing pyroptosis and regulating lactic acid metabolism. *Angew. Chem. Int. Ed.* **62**, e202307706 (2023).
35. Fan, G. et al. Intra/Extracellular lactic acid exhaustion for synergistic metabolic therapy and immunotherapy of tumors. *Adv. Mater.* **31**, 1904639 (2019).
36. Wang, J.-W. et al. A Self-driven bioreactor based on bacterium–metal–organic framework biohybrids for boosting chemotherapy via cyclic lactate catabolism. *ACS Nano* **15**, 17870–17884 (2021).
37. Cao, Z. et al. Lactate oxidase nanocapsules boost T cell immunity and efficacy of cancer immunotherapy. *Sci. Transl. Med.* **15**, eadd2712 (2023).
38. Martínez-Reyes, I. & Chandel, N. Cancer metabolism: looking forward. *Nat. Rev. Cancer* **21**, 669–680 (2021).
39. de Visser, K. & Joyce, J. The evolving tumor microenvironment: from cancer initiation to metastatic outgrowth. *Cancer Cell* **41**, 374–403 (2023).
40. Ren, Y. et al. Multifaceted role of redox pattern in the tumor immune microenvironment regarding autophagy and apoptosis. *Mol. Cancer* **22**, 130 (2023).
41. Li, W.-P. et al. Controllable CO-release following near-infrared light-induced cleavage of iron carbonyl derivatized Prussian blue nanoparticles for CO-assisted synergistic treatment. *ACS Nano* **10**, 11207–11036 (2016).
42. Lyu, M. et al. Personalized carbon monoxide-loaded biomimetic single-atom nanozyme for ferroptosis-enhanced FLASH radioimmunotherapy. *Adv. Funct. Mater.* **33**, 2306930 (2023).
43. Xiao, X. et al. Multifunctional carbon monoxide nanogenerator as immunogenic cell death drugs with enhanced antitumor immunity and antimetastatic effect. *Biomaterials* **277**, 121120 (2021).
44. Askes, S., Reddy, G., Wyrwa, R., Bonnet, S. & Schiller, A. Red light-triggered CO release from $Mn_2(CO)_{10}$ using triplet sensitization in polymer nonwoven fabrics. *J. Am. Chem. Soc.* **139**, 15292–15295 (2017).
45. Ma, G. et al. H_2O_2-responsive NIR-II AIE nanobomb for carbon monoxide boosting low-temperature photothermal therapy. *Angew. Chem. Int. Ed.* **61**, e202207213 (2022).
46. Krysko, D. et al. Immunogenic cell death and DAMPs in cancer therapy. *Nat. Rev. Cancer* **12**, 860–875 (2012).
47. Kazama, H. et al. Induction of immunological tolerance by apoptotic cells requires caspase-dependent oxidation of high-mobility group box-1 protein. *Immunity* **29**, 21–32 (2008).
48. Peter, M. ROS eliminate danger. *Immunity* **29**, 1–2 (2008).
49. Chiang, S.-K., Chen, S.-E. & Chang, L.-C. A dual role of heme oxygenase-1 in cancer cells. *Int. J. Mol. Sci.* **20**, 39 (2018).
50. Szabo, C. Gasotransmitters in cancer: From pathophysiology to experimental therapy. *Nat. Rev. Drug Discov.* **15**, 185–203 (2015).
51. Fang, J. et al. Carbon monoxide, generated by heme oxygenase-1, mediates the enhanced permeability and retention effect in solid tumors. *Cancer Sci.* **103**, 535–541 (2011).
52. Chen, F. et al. Hemin as a general static dark quencher for constructing heme oxygenase-1 fluorescent probe. *Angew. Chem. Int. Ed.* **62**, e202301598 (2023).
53. You, M. et al. Intelligent micro/nanomotors with taxis. *Acc. Chem. Res.* **51**, 3006–3014 (2018).
54. Adrian, J. et al. Chemotactic synthetic vesicles: design and applications in blood-brain barrier crossing. *Sci. Adv.* **3**, e1700362 (2017).
55. Samudra, S. et al. Enzyme molecules as nanomotors. *J. Am. Chem. Soc.* **4**, 1406–1414 (2013).
56. Somasundar, A. et al. Positive and negative chemotaxis of enzyme-coated liposome motors. *Nat. Nanotechnol.* **14**, 1129–1134 (2019).
57. Zhou, Q. et al. Enzyme-activatable polymer–drug conjugate augments tumour penetration and treatment efficacy. *Nat. Nanotechnol.* **14**, 799–809 (2019).
58. Chen, S. et al. Enhanced tumour penetration and prolonged circulation in blood of polyzwitterion–drug conjugates with cell-membrane affinity. *Nat. Biomed. Eng.* **5**, 1019–1037 (2021).
59. Blanco, E., Shen, H. & Ferrari, M. Principles of nanoparticle design for overcoming biological barriers to drug delivery. *Nat. Biotechnol.* **33**, 941–951 (2015).
60. Cho, H. et al. Mitochondria-targeted drug delivery in cancers. *BBA—Mol. Basis Dis.* **1866**, 165808 (2020).
61. Henan, Z. et al. Nanomessenger-mediated signaling cascade for antitumor immunotherapy. *ACS Nano* **8**, 13188–13199 (2021).

62. Ippolito, L., Morandi, A., Giannoni, E. & Chiarugi, P. Lactate: a metabolic driver in the tumour landscape. *Trends Biochem. Sci.* **44**, 153–166 (2018).
63. Colegio, O. et al. Functional polarization of tumor-associated macrophages by tumor-derived lactic acid. *Nature* **513**, 559–563 (2014).

Acknowledgements

This work was supported by the National Natural Science Foundation of China [22477056(Y.S.), 82472379(B.H.)], National Key R&D Program [2019YFA0709200(Y.S.)], the Jiangsu Province Key R&D Program [BE2021373 (Y.S.)], and the State Key Laboratory of Analytical Chemistry for Life Science [5431ZZXM2304 (Y.S.)].

Author contributions

Z.-Y. Liu and X.-W. Luan contributed equally to this work. Y.-J. Song, B.-S. He and Z.-Y. Liu conceived the idea, designed the study, analyzed and interpreted data, and wrote the manuscript. Z.-Y. Liu performed the experiments. X.-W. Luan constructed the plasmid, gave some support on CRISPR/Cas9-related work, and gave some suggestions on the manuscript. Q.-L. Lu, S.-R. Qin and F. Zeng helped perform the cell flow cytometric analysis and discussed the manuscript. Z. Li performed the COMSOL simulation. All authors approved the manuscript.

Competing interests

The authors declare no competing interests.

Additional information

Supplementary information The online version contains supplementary material available at https://doi.org/10.1038/s41467-025-59590-9.

Correspondence and requests for materials should be addressed to Yujun Song.

Peer review information *Nature Communications* thanks the anonymous reviewers for their contribution to the peer review of this work. A peer review file is available.